

Magnetically controlled mass loss from extrasolar planets in close orbits

James E. Owen^{1*} and Fred C. Adams^{2,3†}

¹*Canadian Institute for Theoretical Astrophysics, 60 St. George Street, Toronto, Ontario, M5S3H8, Canada*

²*Michigan Center for Theoretical Physics, Physics Department, University of Michigan, Ann Arbor, MI 48109, USA*

³*Astronomy Department, University of Michigan, Ann Arbor, MI 48109, USA*

19 August 2014

ABSTRACT

We consider the role magnetic fields play in guiding and controlling mass-loss via evaporative outflows from exoplanets that experience UV irradiation. First we present analytic results that account for planetary and stellar magnetic fields, along with mass-loss from both the star and planet. We then conduct series of numerical simulations for gas giant planets, and vary the planetary field strength, background stellar field strength, UV heating flux, and planet mass. These simulations show that the flow is magnetically controlled for moderate field strengths and even the highest UV fluxes, i.e., planetary surface fields $B_P \gtrsim 0.3$ gauss and fluxes $F_{UV} \sim 10^6$ erg s^{−1}. We thus conclude that outflows from *all* hot Jupiters with moderate surface fields are magnetically controlled. The inclusion of magnetic fields highly suppresses outflow from the night-side of the planet. Only the magnetic field lines near the pole are open and allow outflow to occur. The fraction of open field lines depends sensitively on the strength (and geometry) of the background magnetic field from the star, along with the UV heating rate. The net effect of the magnetic field is to suppress the mass loss rate by (approximately) an order of magnitude. Finally, some open field lines do not allow the flow to pass smoothly through the sonic point; flow along these streamlines does not reach steady-state, resulting in time-variable mass-loss.

Key words: magnetohydrodynamics (MHD) — planets and satellites: atmospheres — planets and satellites: formation — planets and satellites: magnetic fields

1 INTRODUCTION

Hot Jupiters make up an important class of extrasolar planets that orbit their parental stars with short periods, roughly in the range $P_{\text{orb}} = 2 - 6$ day. They have masses comparable to Jupiter, $M_P \sim M_J$, and display a wide range of radii and metallicity for a given mass. Although only about $\sim 1\%$ of stars host Hot Jupiters, these objects often transit their stars and hence their properties – in addition to their orbits – can often be measured or constrained. Estimates have been made for their planetary radii, core masses, and even some of their atmospheric properties.

When giant planets orbit their stars with short periods, they can be close enough to experience substantial mass loss. The outflowing gas can absorb UV radiation from the star and thereby increase the inferred radius of the planet’s atmosphere at UV wavelengths, compared to that indicated by the actual planetary radius (which is measured at optical

wavelengths). This effect has been observed in the HD209458 system (starting with Vidal-Madjar et al. 2003), where current estimates indicate a mass loss rate of approximately $\dot{M}_P \approx 8 \times 10^{10}$ g/s (Linsky et al. 2010). In addition, the exoplanet HD189733b has been observed to experience mass loss at a comparable rate $\dot{M}_P \sim 10^{10}$ g/s (Lecavelier des Etangs et al. 2010), and more detections are expected in the near future.

The observed mass loss rates from Hot Jupiters are roughly consistent with those expected from order of magnitude estimates. If the outflow from the planet is controlled by the rate at which the planetary surface gains energy from the star, the mechanical luminosity of the outflow $GM_P\dot{M}_P/R_P$ must be balanced by the energy deposition rate $\eta_{\text{rad}}F_{UV}\pi R_P^2$. Here we assume that stellar UV radiation drives the outflow and introduce a parameter η_{rad} that incorporates the efficiency of energy capture and allows for the radiation to be absorbed above the planetary surface (at R_P). An order of magnitude estimate for the resulting mass

* e-mail: jowen@cita.utoronto.ca

† e-mail: fca@umich.edu

outflow rate \dot{M}_P is then given by

$$\begin{aligned}\dot{M}_P &= \eta_{\text{rad}} \frac{\pi R_P^3 F_{UV}}{GM_P} \\ &\approx 10^{10} \text{ g s}^{-1} \eta_{\text{rad}} \left(\frac{F_{UV}}{450 \text{ erg s}^{-1} \text{ cm}^{-2}} \right) \\ &\times \left(\frac{R_P}{10^{10} \text{ cm}} \right)^3 \left(\frac{M_P}{M_J} \right)^{-1},\end{aligned}\quad (1)$$

where the second equality uses typical values for the planetary properties. The fiducial UV flux $F_{UV} = 450 \text{ erg s}^{-1} \text{ cm}^{-2}$ is the flux appropriate for the quiet Sun at a distance of $a = 0.05 \text{ AU}$ (Woods et al. 1998). This type of estimate has been presented previously (for further discussion, see Waston et al. 1981; Lammer et al. 2003; Baraffe et al. 2006, 2004; and many others). Note that the escape speed from the planetary surface $v_{\text{esc}} \sim 50 \text{ km/s}$, whereas UV radiation generally heats gas up to temperatures $T \sim 10^4 \text{ K}$ (Spitzer 1978; Shu 1992) corresponding to a sound speed $a_s \sim 10 \text{ km/s}$. Since $v_{\text{esc}} > a_s$, outflows are suppressed in that the heated gas is not free to escape, but rather must climb out of its gravitational potential well (e.g., see the discussion of Adams et al. 2004; Owen et al. 2010, 2012 in the context of evaporation from circumstellar disks). More sophisticated planetary outflow models have been constructed, including chemistry, photoionization, and recombination (Yelle 2004; Garcia-Munoz 2007; Koskinen et al. 2007, 2010, 2013), including the effects of tidal enhancement (Erkaev et al. 2007; Murray-Clay et al. 2009), heating from the X-rays (Owen & Jackson 2012) and two-dimensional geometry (Stone & Proga 2009).

This paper considers the problem of mass loss from planets in the presence of magnetic fields from both the star and planet. As shown below, magnetic fields are often expected to dominate the ram pressure of the outflow by many orders of magnitude and cannot be neglected. On the other hand, the effects of magnetic fields on planetary outflows has not been well studied (previous work includes Trammell et al. 2011, 2014; and Adams 2011, hereafter Paper I; see also Laine et al. 2008). Trammell et al. (2014) performed a set of isothermal ideal MHD simulations that included a dipole planetary field, along with rotation and the tidal field. These simulations did not include radiative transfer and the mass-loss rates were controlled by the ‘base-density’ prescribed in the simulation domain’s inner boundary. The results of these simulations followed the analytic predictions of Paper I and semi-analytic predictions of Trammell et al. (2011). Namely, that for sufficiently strong magnetic fields outflow is confined to occur along the open field lines (from the poles) and that equatorial regions can contain a large ‘dead-zone’ which is in magneto-static equilibrium. Trammell et al. (2014) found this configuration resulted in a markedly reduced mass-loss rate compared to a pure hydrodynamic setup, where outflow can occur from the equatorial regions of the planet.

This work extends these earlier treatments in a number of ways: importantly we present the first multi-dimensional calculations that include EUV radiative transfer; additionally we also include more complex and realistic geometries for the magnetic fields, extend the parameter space under study, and by provide additional analytic calculations to help interpret the numerical results.

In addition to planetary outflows, however, a related

body of work exists concerning the interactions between planetary magnetospheres and those of the stars (starting with Cuntz et al. 2000). The observational signatures of star-planet interactions include cyclic variations of stellar activity that have the same period as the planetary orbit; such signatures have been observed, but are often intermittent (Shkolnik et al. 2005, 2008).

This paper is organized as follows. Section 2 outlines the different regimes of parameter space for planetary outflows, and defines the regime of interest here. The outflow problem is formulated in Section 3, along with an overview of our numerical approach. Next we derive a collection of supporting analytic results, including a derivation of the fraction of the planetary surface that supports open field lines (in Section 4). Our main numerical results are then presented in Section 5, including the suppression of outflow on the night side of the planet and due to lack of open field lines. Finally, we conclude in Section 6 with a summary and discussion of our results, along with a roadmap for further work.

2 PARTITIONS OF PARAMETER SPACE

Both the star and the planet have magnetic fields (with surface strengths B_* and B_P , respectively) and outflows with mass loss rates \dot{M}_* and \dot{M}_P . The relative strength of these quantities determines the regime of parameter space in which the planetary wind is launched. This section outlines the expected extent of this parameter space. To leading order the magnetic field, on both bodies, is taken to have a dipole form (note that we consider the departures from this idealized case below). As a result, for purposes of outlining the parameter space, we consider the field strength to scale with distance according to the simple law

$$B = |\mathbf{B}| \sim B_0 \left(\frac{R_0}{r} \right)^3. \quad (2)$$

This form holds for both the star or the planet, where R_0 is the radius of the body, B_0 is the surface field strength, and the origin of the coordinate system(s) lies at its center. The mass loss rate from either the star or the planet is constant (with radius) and obeys the continuity condition

$$\dot{M} = 4\pi r^2 \rho v, \quad (3)$$

where the density $\rho(r)$ and flow speed $v(r)$ depend on the radial coordinate.

2.1 Dimensionless Parameters for Single Bodies

For both the star and the planet, we can define a dimensionless parameter Λ that measures the ratio of ram pressure from the outflow to the magnetic field pressure. This quantity is a function of the radial distance r from the body and can be written in the form

$$\Lambda \equiv \frac{2\dot{M}v}{B^2 r^2}. \quad (4)$$

The radial dependence of the magnetic field strength B is given by equation (2), the outflow rate \dot{M} is constant, and the outflow speed v is expected to be of order the sound speed at the locations of interest. As a result, to leading order, the parameter Λ scales with radius according to

$\Lambda \sim r^4$. To higher order, the outflow speed is a slowly increasing function of radius and the magnetic field decreases less steeply than indicated by equation (2), so that Λ increases somewhat more slowly than this simple scaling.

For the star, the dimensionless parameter Λ_* takes the form

$$\Lambda_* \approx 0.004 \left(\frac{\dot{M}_*}{10^{12} \text{g/s}} \right) \left(\frac{v_*}{100 \text{km/s}} \right) \left(\frac{B_*}{1 \text{G}} \right)^{-2} \times \left(\frac{R_*}{R_\odot} \right)^{-2} \left(\frac{r}{R_*} \right)^4, \quad (5)$$

where the fiducial parameters values are chosen to be comparable to those of the solar wind. Note that we use $v_* = 100$ km/s as the fiducial outflow speed; the asymptotic value is larger, $v_\infty \sim 400$ km/s, but the solar wind speed is smaller at the radial distances characteristic of Hot Jupiter orbits. The dimensionless parameter Λ_* is expected to exceed unity at a nominal radius $r \sim 4R_*$. Since 4-day orbits correspond to semi-major axes $a \sim 10R_*$, the parameter Λ_* will often exceed unity at the location of the planet. However, the outflow rate from the star can be smaller (perhaps by a factor of 10) and the surface field strength can be larger (by another factor of 10), so that the parameter Λ_* can remain less than unity out to a radius $r \sim 22R_*$, well beyond the orbits of Hot Jupiters. As a result, the parameter space of interest includes both systems where the stellar wind opens up the stellar magnetic field and systems where the field lines remain closed (at the location of the planet).

For the planet itself, the corresponding parameter takes the form

$$\Lambda_P \approx 2 \times 10^{-4} \left(\frac{\dot{M}_P}{10^{10} \text{g/s}} \right) \left(\frac{v_P}{10 \text{km/s}} \right) \left(\frac{B_P}{1 \text{G}} \right)^{-2} \times \left(\frac{R_P}{10^{10} \text{cm}} \right)^{-2} \left(\frac{r}{R_P} \right)^4, \quad (6)$$

where we have used fiducial parameters appropriate for Hot Jupiters. The dimensionless parameter Λ_P is a function of radius and exceeds unity at $r \sim 8.4R_P$. As shown below, the sonic point for the planetary wind typically falls at $r \sim 3R_P$, so that the parameter Λ_P will often remain less than unity for the launch of the outflow. The planetary field strength can be even larger, perhaps $B_P \approx 10$ G, which would increase the crossover radius out to $r \sim 27R_P$. On the other hand, for surface field strengths $B_P \lesssim 0.1$ G, the crossover radius can fall within the sonic surface. Since this paper focuses on magnetically controlled flow, these calculations are only applicable for Jovian planets with surface fields $B_P \gtrsim 0.1$ G.

A partition of parameter space can be made by considering the four choices

$$\begin{aligned} \Lambda_* < 1, \Lambda_P > 1 & \quad \Lambda_* < 1, \Lambda_P < 1, \\ \Lambda_* > 1, \Lambda_P > 1 & \quad \Lambda_* > 1, \Lambda_P < 1. \end{aligned} \quad (7)$$

For cases corresponding to the top row in equation (7), where $\Lambda_* < 1$, the stellar magnetic field dominates the stellar wind at the location of the planet, and the stellar field is essentially a dipole. In this case, the most likely configuration is for the planet to orbit in the equatorial plane of the star, with its pole aligned with the orbit. The magnetic field lines of the star will be essentially vertical, in the \hat{z} direction of the planet. One complication that arises in this

case is that the dipoles of the star and planet can either be aligned or anti-aligned. Another complication is that the star will not, in general, rotate with the same angular velocity as the planetary orbit. As a result, the field lines from the star will tend to wrap up.

For cases corresponding to the bottom row in equation (7), where $\Lambda_* > 1$, the stellar wind dominates over the stellar magnetic field at the location of the planet. The stellar wind and the stellar magnetic field will thus be (nearly) radial at this position (where a radial magnetic field has a split-monopole configuration). The stellar wind and stellar magnetic field scale as $(r/R_*)^2$ and $R_* \gg R_P$, so that both are essentially constant in the vicinity of the planet, i.e., they can be considered constant when studying the launch of the planetary outflow. In addition, the angular momenta of both the spin and orbit of the planet are likely to be (nearly) perpendicular to the equatorial plane of the star. One likely geometry is thus for the stellar field (and wind) to point sideways with respect to the pole of the planet. However, many other geometries are possible. Another natural case to consider is where the planet is tipped sideways so that the pole of the planet aligns with the radial direction of the star, and hence with the direction of both the stellar wind and stellar magnetic field.

For cases corresponding to the right hand sides of equations (7), the planetary magnetic field is stronger than the ram pressure of the planetary outflow. In this case, the launch of the planetary outflow is constrained to follow the magnetic field lines, which will (in general) be modified to include the stellar field. If the stellar field is stronger than the stellar wind (at the location of the planet), the stellar field produces a nearly vertical contribution and the launch of the wind can be described using the formalism developed in Paper I. If the stellar wind overwhelms the stellar field at the planet location, then the field lines from the planet must join onto the nearly radial (and hence nearly horizontal) field lines from the star.

For the left hand sides of equations (7), the planetary outflows have greater ram pressure than the planetary magnetic fields. In this case, the planetary magnetic fields become nearly radial near the planet and the flow is nearly spherical. After leaving the vicinity of the planet, this (nearly) spherical flow must then join onto the environment of the star, either a dipole field that connects to the stellar pole, or a nearly radial flow that joins onto the stellar wind (where this latter radial flow is centered on the star).

2.2 Dimensionless Parameters for Star-Planet Interactions

Next we define a collection of parameters that characterize how the winds and magnetic fields of stars interact with the winds and magnetic fields of the planets. For the cases where the stellar wind dominates over the stellar magnetic field, we must determine how the ram pressure from the stellar wind compares to the ram pressure from the planetary wind and to the magnetic field pressure from the planet. The ratio of the stellar wind ram pressure, evaluated at the location of the planet, to the ram pressure of the planetary wind is given by

$$\Pi_{WW} = \frac{\dot{M}_* v_* r^2}{\dot{M}_P v_P a^2} \approx 0.10 \frac{r^2}{R_P^2}, \quad (8)$$

where r is the radial coordinate centred on the planet and a is the semimajor axis of the planetary orbit. For most applications we can take the orbit to be nearly circular, so that a is also the distance to the star. Here we expect $\dot{M}_*/\dot{M}_P \sim 100$, $v_*/v_P \sim 10$, and $a/R_P \sim 100$, which leads to the numerical value on the right hand side of equation (8). Using the approximate scaling law from equation (1), we expect the planetary outflow rate to scale as $\dot{M}_P \sim F_{UV} \sim a^{-2}$, so that the parameter Π_{WW} should be independent of planetary semi-major axis a to leading order. With these fiducial values for the system properties, the planetary outflow becomes weaker than the background outflow from the star at a radius $r \approx 3.2R_P$, measured from the planet, a location that falls near the expected sonic surface.

Similarly, we find the ratio of the ram pressure from the stellar wind, again evaluated at the location of the planet, to the pressure provided by the planetary magnetic field. This ratio takes the form

$$\Pi_{WB} = \frac{2\dot{M}_* v_*}{B_P^2 a^2} \left(\frac{r}{R_P} \right)^6 \approx 3.6 \times 10^{-5} \left(\frac{r}{R_P} \right)^6, \quad (9)$$

where r is the radial coordinate centered on the planet. For the fiducial parameter values, the ratio $\Pi_{WB} = 1$ for $r \approx 5.5R_P$, i.e., somewhat outside the expected location of the sonic surface. This radius (where $\Pi_{WB} = 1$) corresponds to the magnetopause for the planet.

For cases where the magnetic field of the star is strong enough to guide the stellar wind, the stellar field must be compared to both the planetary wind and the planetary magnetic field. The ratio of the two magnetic fields thus provides a third dimensionless parameter that can be written (approximately) in the form

$$\Pi_{BB} = \left(\frac{B_*}{B_P} \right)^2 \left(\frac{r}{R_P} \right)^6 \left(\frac{R_*}{a} \right)^6 \approx 10^{-6} \left(\frac{r}{R_P} \right)^6, \quad (10)$$

where r is the radial coordinate centered on the planet and a is the distance to the star. The magnetic sphere of influence of the planet thus extends out to $r \sim 10R_P$. Note that this scaling uses equation (2) is thus approximate; specific magnetic field configurations, for both the star and planet, will result in modified (and non-spherical) boundaries.

To complete the set, we define Π_{BW} to be the ratio of the magnetic field pressure provided by the star to the ram pressure of the planetary wind,

$$\Pi_{BW} = \frac{B_*^2 r^2}{2\dot{M}_P v_P} \left(\frac{R_*}{a} \right)^6 \approx 5 \times 10^{-3} \left(\frac{r}{R_P} \right)^2, \quad (11)$$

where we have used typical values (see above) to evaluate the ratio in the second equality. With these values, the stellar magnetic field does not play a role within $r \sim 14R_P$. Keep in mind that the the magnetic field from the star is evaluated at the location of the planet and hence depends sensitively on the distance a between the two bodies. Since we expect $\dot{M}_P \sim a^{-2}$ (see equation [1]), the parameter $\Pi_{BW} \sim a^{-4}$ (for a dipole scaling dependence of the stellar field). Notice also that $\Pi_{BW}\Pi_{WB} = \Pi_{BB}\Pi_{WW}$, so that the four quantities Π_{jk} are not independent.

Equations (8 – 11) indicate that the planetary magnetic field often tends to protect the planetary outflow, at least un-

til the outflow passes through the sonic surface. After passing through the sonic point, however, the flow must join onto the larger scale geometry that is determined by the interplay between the stellar magnetic field and the stellar wind. In any case, it is useful to separate the launching of the wind from its propagation at larger distances from the planet. In particular, the launch of the wind will often take place under conditions where the planetary magnetic fields are strong enough to guide the flow. However, the background magnetic field provided by the star is generally strong enough to affect the detailed shape of the field lines and can influence the flow at the sonic surface. In some cases, the stellar field not only changes the location of the sonic points, but can also prevent the flow from passing smoothly through the sonic transition (Paper I).

2.3 Time Dependence

The mass loss rates for solar-type stars are expected depend on stellar age, so that the rate \dot{M}_* has an approximate time-dependence of the form

$$\dot{M}_*(t) = \dot{M}_{*0} \left(\frac{t_w}{t_w + t} \right)^2, \quad (12)$$

where $t_w \approx 0.1$ Gyr and $\dot{M}_{*0} \approx 2 \times 10^{-11} M_\odot \text{ yr}^{-1}$ (Wood et al. 2002). Note that the starting mass loss rate is about 2000 times the current value for the Sun. This benchmark mass loss rate is somewhat larger than the values ($\dot{M} \sim 10^{-13} M_\odot \text{ yr}^{-1}$) considered “typical” for weak-lined T Tauri stars (e.g., Guenther & Emerson 1997). On the other hand, this initial mass loss rate \dot{M}_{*0} is somewhat smaller than the rates expected for classical T Tauri stars; these object exhibit a wide range of values $\dot{M} \sim 10^{-8} - 10^{-10} M_\odot \text{ yr}^{-1}$ (e.g., Hartigan et al. 1995). We thus expect equation (12) to provide a good estimate for the average mass loss rates as a function of time, but the variance will be large for early times (especially the T Tauri phases).

The magnetic field strength is observed to scale (roughly) with the stellar rotation rate, and both decrease with time. One version of this scaling law is a magnetic Bode’s law (Baliunas et al. 1996), which shows that the stellar magnetic moment scales with the stellar angular momentum, so that we expect a scaling law of the general form

$$B_* \sim \Omega_*^{1/2} \quad \text{where} \quad \Omega_* \sim t^{-1/2}, \quad (13)$$

where the second expression is the well-known relationship for spin-down of stars (Skumanich 1972). Taken together, these two results indicate that $B_* \sim t^{-a}$, where the index $a \approx 1/4$. Since the stellar mass loss rates scales as $\dot{M}_* \sim t^{-2}$, and $B_*^2 \sim t^{-1/2}$, the dimensionless parameter $\Lambda_* \sim t^{-3/2}$. This result would indicate that Λ_* would be larger in the past. However, this scaling only applies to relatively old stars, i.e., these results cannot be extrapolated back to the early pre-main-sequence phases.

In contrast, T Tauri stars, with ages of a few Myr, have surface fields $B_* \sim 2500$ G (Johns-Krull 2009). These young stars often have substantial components of their magnetic field in higher order multipoles (Gregory et al. 2010; Gregory 2011), whereas only the dipole component is relevant at the location of the planets. Nonetheless, the dipole component is still expected to have a large field strength of $B \sim 1000$

G. Compared to Solar values, T Tauri stars thus have values of B_*^2 that are larger by a factor of $\sim 10^6$, but the outflow rates are larger, on average, by only a factor of ~ 2000 . This scaling would indicate that the parameter Λ_* is smaller for young stars by a factor of ~ 1000 . But weak-line T Tauri stars have outflow rates that are weaker than this average value, and hence have even smaller values of Λ_* . Classical T Tauri stars can produce much larger outflow rates, more than 10^6 times the current Solar value, and could thus have smaller values of Λ_* .

Taken together, the above results indicate that the values of the dimensionless parameters (Λ, Π) are likely to vary substantially with the age of the star/planet system. Further, these parameters can be either larger or smaller in the past, and are expected to vary from system to system.

3 FORMULATION OF THE OUTFLOW PROBLEM

For the sake of definiteness, we consider a simple magnetic field configuration consisting of two components. The planet has a dipole field with strength B_P . In addition, the stellar field at the location of the planet has a contribution that we model as a constant field that points along the pole of the planet, i.e.,

$$\mathbf{B} = \beta_* B_P \hat{\mathbf{z}} \quad \text{where} \quad \beta_* \equiv \frac{B_*}{B_P} \left(\frac{R_*}{a} \right)^3, \quad (14)$$

where B_P and B_* are the surface field strengths on the planet and the star, respectively. With this choice of stellar field component we have restricted ourselves to cases where $\Lambda_* < 1$. Additionally, we assume that this stellar field structure protects the planet from the stellar wind, again restricting ourselves to the region of parameter space where $\Pi_{WW} \ll 1$. Thus, we do not include a stellar wind component in our detailed calculations. Therefore, the aim of this initial study is to investigate the interplay between the magnetic field strength and structure and the evaporative flow (i.e., varying Λ_P and Π_{BW}). Specifically, we aim to understand under what conditions the launching of the evaporative flow is controlled by the magnetic field ($\Lambda_P \ll 1$, $\Pi_{BW} \ll 1$) or the evaporative flow is strong enough to fully disrupt the magnetic field structure allowing quasi-spherical outflow ($\Lambda_P \gg 1$, $\Pi_{BW} \gg 1$). For cases where the magnetic field controls the flow geometry, planetary mass-loss can be significantly suppressed relative to the quasi-spherical outflows (see Paper I) that are commonly used in modelling planetary evaporation (e.g. Lammer et al. 2003; Koskinen et al. 2007; Murray-Clay et al. 2009; Owen & Jackson 2012).

Even with our restricted choice of interest, the parameter space for planetary outflows is large. We must specify the planet properties, including the planetary mass M_P , radius R_P , and surface field strength B_P . We must also specify the stellar properties that define the environment that the planet resides within, i.e., the background stellar field strength (determined by the parameter β_*) and the stellar UV flux F_{UV} evaluated at the location of the planet. For most of this work, we focus on Hot Jupiters with mass $M_P = 1.0 M_J$ and $R_P = 10^{10}$ cm, although we vary the planet mass for one series of simulations. Note that this value for the radius is somewhat larger than that of

Jupiter itself, where this radius anomaly is well known for Hot Jupiters (Bodenheimer et al. 2003; Laughlin et al. 2011). With these choices, the relevant parameter space is given by (B_P, β_*, F_{UV}) .

In this work we consider both numerical calculations and analytic studies, with a focus on the latter. We use supporting analytic calculations as a guide to explore the underlying physics and interpret the results of the numerical calculations, as well as to draw inferences out of the range of our simulations. As a result, for our analytic work we follow Paper I and consider the magnetic field to be static and force-free (and this approximation is largely vindicated by the numerical simulations). In our numerical calculations we do not evolve the full energy equation and instead use a simplified thermal update (Gritschneider et al. 2009). This simplification restricts our initial calculations presented within to the radiative-recombination regime (Murray-Clay et al. 2009) and as such high UV fluxes ($\gtrsim 10^5$ erg s $^{-1}$). Additionally evolving the energy equation in multi-dimensions with ionizing chemistry and radiative transfer is computationally challenging and will be done in our next study.

3.1 Numerical Calculations

In the numerical studies we solve the Radiation-MHD problem in the ideal MHD limit (i.e., the magnetic structure is allowed to respond to the flow). In addition to the standard ideal-MHD equations, we additionally evolve the ionization fraction in the flow and the radiative transfer problem for ionizing photons. The time evolution of the ionization fraction is given by

$$\frac{DX}{Dt} = (1 - X)(\Gamma + n_e C) - X n_e \alpha_r, \quad (15)$$

where X is the ionization fraction, n_e is the electron density, Γ is the photoionization rate, C is the collisional ionization rate, and α_r is the recombination rate. We calculate the photoionization rate Γ assuming a monochromatic spectrum with a frequency of $h\nu_{13.6} = 13.6$ eV, such that

$$\Gamma = \frac{F_{UV}}{h\nu_{13.6}} \sigma_{13.6} \exp(-\tau), \quad (16)$$

where $\sigma_{13.6}$ is the photoionization cross section at energy $h\nu_{13.6} = 13.6$ eV (Osterbrock 1989). Additionally, τ is the optical depth to ionizing photons and is defined according to

$$\tau = \sigma_{13.6} N_{HI}, \quad (17)$$

where N_{HI} is the neutral Hydrogen column density.

Our choice of a monochromatic spectrum at 13.6 eV is chosen for numerical convenience. However, since our parameter range of interest is in the recombination balance regime the chosen photon energy does not control the level of heating/ionization in our setup. It is merely the number (rather than their energy) of ionizing photons that controls the level of ionization and hence the mass-loss rates. This approximation obviously cannot be extended to arbitrarily low UV fluxes (but such low fluxes are not considered here). Murray-Clay et al. (2009) choose a characteristic energy of 20 eV. Thus, there is a small correction factor in the number of ionizing photons of 1.47 when comparing fluxes in terms of energy per-unit time and a small difference in the mass-loss rates (which goes approximately as the square-root of

the number of ionizing photons) of 1.2, much smaller than the differences we find due to the presence of the magnetic fields.

Our numerical calculations are performed using a modified version of the ZEUS-MP MHD code (Stone & Norman 1992a,b; Hayes et al. 2006), where we additionally solve equation (15), along with the radiative transfer of ionizing EUV photons. Our radiative transfer scheme is detailed in Appendix A and our numerical approach is described in detail in Appendix B. Essentially, we assume that the recombination time is short compared to the flow time and the ionizing photons have a mean-free path that is short compared to the flow length-scale at the ionization front. As such, this set of assumptions restricts us to the largest UV fluxes ($\gtrsim 10^5$ erg s $^{-1}$), where the gas is close to radiative-recombination equilibrium; however, it allows us to simplify the thermal structure in the flow where ionized gas is assumed to be isothermal at 10^4 K and neutral gas is taken to be isothermal at 10^3 K. We stress that this restriction in EUV flux does not prevent us achieving our goal for this work: Any outflow that is magnetically dominated at high fluxes, will also be magnetically dominated at lower fluxes since the mass-loss rate increases with increasing flux.

All of the numerical calculations are performed on a 2D spherical grid (r, θ). Note that for the simulation where we include both the day and night side of the planet, the use of a 2D grid involves a greater degree of approximation and cannot be considered globally axisymmetric (see Section 5.1). We emphasise that planetary evaporation is a fundamentally 3D process. In particular, rotation cannot be included in our simulations with both a day and night side as this would violate the ‘pseudo-symmetry’ of our setup. Furthermore, the centrifugal force cannot be included at all in such a simulation; however, it is expected to be very small in planetary evaporation (Stone & Proga 2009; Murray-Clay et al. 2009; Owen & Jackson 2012). In all cases we take the symmetry axis of the planetary dipole to be perpendicular to the orbital plane. Additionally any contribution from the stellar magnetic field $\beta_* > 0$ is also assumed to be perpendicular to the orbital plane (see Equation 14). In our plots we adopt the standard Cartesian to spherical co-ordinate system mapping, with the z-axis taken to be the symmetry axis of the dipole and the star is located along the positive x-axis. Our computational domain has an inner boundary at 10^{10} cm and at outer boundary at 1.5×10^{11} cm. For reference, note that the sonic radius for an isothermal (10^4 K), spherical flow is $\sim 3 \times 10^{10}$ cm for a Jupiter mass planet. The radial grid is non-uniform and is of size $N_r = 128$, where the resolution at the inner boundary has approximately 100 km sized cells, sufficient to resolve the scale height of the underlying bolemetrically heated atmospheres. In the angular direction we use a uniform grid with 64 cells per quadrant. At the inner boundary we apply fixed boundary conditions where the density is set to 10^{-11} g cm $^{-3}$, the temperature is set to 10^3 K, magnetic field is set to a dipole of strength B_P , and the ionization fraction is set to $X = 10^{-5}$. On the outer boundary we adopt outflow boundary conditions, but include the contribution from the background stellar field if $\beta_* > 0$. Finally, on the angular boundaries we adopt the appropriate symmetry boundary conditions. In order to isolate the effects of the magnetic field, we neglect the small contri-

butions from planetary rotation and the stellar gravitational field.

We initialise the simulations to be isothermal at 10^3 K, with a hydrostatic density structure close to the planet. At larger radii we fill the grid with a low density gas (which is optically thin to 13.6 eV photons) that falls off with density as $\rho \sim r^{-2}$; this density profile is normalized such that the plasma beta in the grid is larger than 10^{-4} in order to prevent very short numerical time-steps. This radius where we transfer from the hydrostatic density structure to the power-law fall off depends on the initial magnetic field strength, but typically occurs around ~ 2 planetary radii. Note that, in general, our simulations evolve towards steady-state solutions, so that this initial density structure is purely a matter of convenience. We then evolve the flow system for ~ 15 flow crossing times. Unless specifically stated otherwise, all of the results from the simulations described herein are measured after 13 flow crossing times. In general, the flow reaches steady-state after only 2 – 3 flow crossing times.

4 ANALYTIC EXPECTATIONS: MAGNETIC LOOPS AND OPEN FIELDS LINES

This section calculates the hydrostatic structure of coronal plasma following magnetic loops on planetary surfaces, we can then use this result to understand under what limits the flow will be controlled by planet’s dipole. The formulation is general, but the application is made for Hot Jupiters. We start by considering dipole magnetic field configurations, but the results can be generalized to include quadrupole, octupole, and more general cases (although this approach is limited to cases with azimuthal symmetry). More specifically, we find analytic expressions for the shape of the magnetic field lines, the coordinates following the field lines, and the pressure integrated along the field lines. These results are then used to determine the fraction of the surface that supports closed field lines, the radial extent of the loops, and the corresponding volume of the trapped magnetic region.

4.1 Basic Formulation

For a rotating system, the effective gravity \mathbf{g} is given by

$$\begin{aligned} \mathbf{g} &= (g_r, g_\theta, g_\phi) \\ &= \left(-\frac{GM_P}{r^2} + \Omega^2 r \sin^2 \theta, \Omega^2 r \sin \theta \cos \theta, 0 \right), \end{aligned} \quad (18)$$

where Ω is the planetary rotation rate, and where the rotation axis coincides with the \hat{z} direction of the coordinate system. Note that this analytic treatment includes rotational effects ($\Omega \neq 0$) so that we can assess their importance. Since rotational effects are small (see below), in our numerical treatment (see the following section) we neglect rotation in order to isolate the effects of the magnetic fields.

We assume that the plasma is isothermal with sound speed a_s . As discussed above the temperature is expected to be about $T_C \sim 10^4$ K and the magnetic field strengths are typically in the range $B = 1 - 10$ G. The sound speed is thus $a_s \sim 10$ km s $^{-1}$.

If we assume that the coronal plasma is in hydrostatic equilibrium, the pressure along a given magnetic loop takes the form

$$P(s) = P_0 \exp \left[\frac{1}{a_s^2} \int_0^s \mathbf{g} \cdot \hat{\mathbf{s}} ds \right], \quad (19)$$

where the integral starts at the planetary surface and continues to the point s along the magnetic loop. One can show that

$$\mathbf{g} \cdot \hat{\mathbf{s}} ds = \frac{1}{B} \mathbf{g} \cdot \mathbf{B} ds = g_r dr + \frac{B_\theta}{B_r} g_\theta dr. \quad (20)$$

The pressure integral then becomes

$$P(s) = P_0 \exp \left[\frac{1}{a_s^2} \left(\int_{R_P}^r g_r dr + \int_{R_P}^r \frac{B_\theta}{B_r} g_\theta dr \right) \right]. \quad (21)$$

In order to determine the pressure, we must evaluate the integrals

$$I_1 = \frac{1}{a_s^2} \int_{R_P}^r \left(-\frac{GM_P}{r^2} \right) dr = \frac{GM_P}{a_s^2 R_P} \left(\frac{R_P}{r} - 1 \right), \quad (22)$$

$$I_2 = \frac{1}{a_s^2} \int_{R_P}^r \Omega^2 r \sin^2 \theta dr, \quad (23)$$

and

$$I_3 = \frac{1}{a_s^2} \int_{R_P}^r \frac{B_\theta}{B_r} \Omega^2 r \sin \theta \cos \theta dr. \quad (24)$$

Next we define dimensionless quantities

$$\Phi_g \equiv \frac{GM_P}{R_P a_s^2}, \quad \Phi_c \equiv \frac{1}{2} \left(\frac{\Omega R_P}{a_s} \right)^2, \quad \text{and} \quad \xi \equiv \frac{r}{R_P}. \quad (25)$$

If we take typical parameters so that $M_P = 1.0 M_J$, $R_P = 10^{10}$ cm, $a_s = 10$ km s $^{-1}$, and period $P_{rot} = 4$ days, then $\Phi_g \sim 13$ and $\Phi_c \sim 0.017$. The parameters of this problem thus obey the ordering

$$\Phi_c \ll 1 \ll \Phi_g. \quad (26)$$

We next note that

$$I_1 = \Phi_g \left(\frac{1}{\xi} - 1 \right), \quad (27)$$

so that I_1 is the same for all magnetic field configurations. The remaining two integrals have the form

$$I_2 = \Phi_c J_2 \quad \text{where} \quad J_2 = 2 \int_1^\xi \sin^2 \theta \xi d\xi, \quad (28)$$

and

$$I_3 = \Phi_c J_3 \quad \text{where} \quad J_3 = 2 \int_1^\xi \frac{B_\theta}{B_r} \sin \theta \cos \theta \xi d\xi. \quad (29)$$

We thus need to evaluate J_2 and J_3 for a given form of the magnetic field configuration. Note that along each field line, the angle θ depends on the dimensionless radius ξ , as determined by the field geometry. Once all of the dimensionless integrals have been evaluated, the pressure is then given by

$$P(s) = P_0 \exp \left[\Phi_g \left(\frac{1}{\xi} - 1 \right) + \Phi_c (J_2 + J_3) \right]. \quad (30)$$

As we show below for dipole field configurations, the dimensionless integrals J_2 and J_3 combine to take the form

$$J_2 + J_3 = x^2 - x_P^2, \quad (31)$$

where $x = \xi \sin \theta$ is evaluated at the field point (ξ, θ) and where x_P is the coordinate at the planetary surface that connects to the field point along a magnetic field line.

4.2 Dipole Field Configurations

For the case of dipole fields, the magnetic field components have the form

$$B_r = B_0 \xi^{-3} 2 \cos \theta \quad \text{and} \quad B_\theta = B_0 \xi^{-3} \sin \theta \quad (32)$$

where we have defined $\xi = r/R_P$. The magnetic field lines follow lines of constant values of the coordinate ‘ q ’ (e.g., Adams & Gregory 2012; Adams 2011), so that

$$q = \xi^{-1} \sin^2 \theta = \sin^2 \theta_0 = \text{constant}. \quad (33)$$

The constant q is thus determined by the polar angle (θ_0) of the loop at the planetary surface (the location of the foot-point). With these specifications, the integral J_2 becomes

$$J_2 = 2 \int_1^\xi \sin^2 \theta \xi d\xi = 2q \int_1^\xi \xi^2 d\xi = \frac{2}{3} q (\xi^3 - 1). \quad (34)$$

Similarly, the integral J_3 becomes

$$\begin{aligned} J_3 &= 2 \int_1^\xi \frac{\sin \theta}{2 \cos \theta} \sin \theta \cos \theta \xi d\xi = \int_1^\xi \sin^2 \theta \xi d\xi \\ &= q \int_1^\xi \xi^2 d\xi = \frac{q}{3} (\xi^3 - 1). \end{aligned} \quad (35)$$

As a result, the sum of the two integral simplifies to the form

$$J_2 + J_3 = q (\xi^3 - 1) = x^2 - x_P^2, \quad (36)$$

where x_P is the value at the planetary surface. The pressure can then be written

$$P(\xi) = P_0 \exp \left[\Phi_g \left(\frac{1}{\xi} - 1 \right) + \Phi_c q (\xi^3 - 1) \right]. \quad (37)$$

The planetary surface will support both closed field lines and open field lines, with a critical magnetic field line delineating the boundary between them. We can set the value of the critical streamline, labeled by q_m , by requiring that the magnetic pressure is greater than the gas pressure (from equation [37]) at all points along the critical field line. At the point of equality,

$$\begin{aligned} P_0 \exp \left[\Phi_g \left(\frac{1}{\xi} - 1 \right) + \Phi_c q (\xi^3 - 1) \right] &= \\ \frac{B_0^2}{8\pi} (4 \cos^2 \theta + \sin^2 \theta) \xi^{-6}. \end{aligned} \quad (38)$$

In general, the magnetic field pressure decreases faster than the gas pressure, so we want to evaluate the above expression at the largest radius ξ of the magnetic loop. For dipole fields, considered here, the largest value of the radius is given by $\xi = 1/q$, which occurs where $\sin \theta = 1$ and $\cos \theta = 0$ (along the equator). The above equation becomes

$$\Phi_g (q - 1) + \Phi_c (q^{-2} - q) = \log \left[\frac{B_0^2}{8\pi P_0} \right] + 6 \log q. \quad (39)$$

One must solve the transcendental equation (39) to find the critical value of the variable $q = q_m$ that labels the critical magnetic field line. The result depends on the values of Φ_g and Φ_c , as defined above, as well as the ratio κ of the magnetic field pressure to the gas pressure at the planetary surface (the base of the magnetic loop). Specifically we define

$$\kappa \equiv \frac{B_0^2}{8\pi P_0}. \quad (40)$$

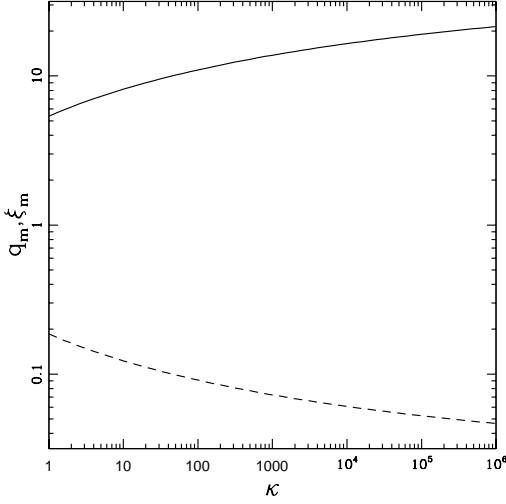


Figure 1. Coordinate q_m of the critical magnetic field line (dashed curve) and the corresponding maximum radial extent ξ_m of the flux loop (solid curve). Both quantities are plotted versus the parameter $\kappa = B_0^2/(8\pi P_0)$, which measures the relative strength of the magnetic field at the planetary surface. The potentials have fixed values $\Phi_g = 13$ and $\Phi_c = 0.017$.

For fixed values of $\Phi_g = 13$ and $\Phi_c = 0.017$, Figure 1 shows the maximum radial extent of the loops as a function of the parameter κ . If we take the limit $\Phi_c \rightarrow 0$ and then consider $q \ll 1$, equation (39) can be solved for the critical value of the coordinate, i.e.,

$$q_m \approx \kappa^{-1/6} \exp[-\Phi_g]. \quad (41)$$

The critical value of the coordinate q_m corresponds to a critical value of the polar angle θ_m on the planetary surface, i.e.,

$$q_m = \sin^2 \theta_m. \quad (42)$$

The fraction F_{AP} of the planetary surface that supports open field fields is given by

$$\begin{aligned} F_{AP} &= 1 - \cos \theta_m = 1 - (1 - \sin^2 \theta_m)^{1/2} \\ &= 1 - (1 - q_m)^{1/2}, \end{aligned} \quad (43)$$

which reduces to the approximate form

$$F_{AP} \approx \frac{1}{2} \kappa^{-1/6} \exp[-\Phi_g/6]. \quad (44)$$

This fraction F_P corresponds to the the open field lines produced due to the hot plasma opening up the magnetic field, which has a purely dipole form. For the case where the field also has a (straight) background component (e.g., due to the star), a fraction of the planetary surface will support open field lines even in the limit of zero temperature. This fraction F_{BP} is given by (see Paper I)

$$F_{BP} = 1 - \left[1 - \frac{3\beta_*^{1/3}}{2 + \beta_*} \right]^{1/2} \approx \frac{3}{4} \beta_*^{1/3}, \quad (45)$$

where the second equality assumes $\beta_* \ll 1$.

By comparing equations (44) and (45), we can determine which process is dominant in producing open field lines, thermal opening of magnetic loops or the underlying field geometry (including the stellar background field). Since $\Phi_g \sim 10-12$, the fraction $F_{AP} \sim 0.1 \kappa^{-1/6}$, whereas the fraction $F_{BP} \sim 0.1$ (since the parameter $\beta_* \sim 0.001$). In most cases, more field lines are open due to the background stellar field than are opened up by the plasma pressure. However, the latter effect scales as $\kappa^{1/6}$ so that sufficiently hot plasma temperatures can also lead to additional open field lines. In general, the ratio of the two areas is given by

$$\frac{F_{BP}}{F_{AP}} = \frac{3}{2} \exp[\Phi_g/6] \beta_*^{1/3} \kappa^{1/6} \approx 11 \beta_*^{1/3} \kappa^{1/6}. \quad (46)$$

Next we note that $\kappa \sim B_P^2$ and $\beta_* \sim B_*/B_P$, where B_P is the surface field strength on the planet, so that the ratio is independent of the planetary field strength. However, this expression is only valid in the regime where the planetary field strength is large enough to control the flow; in practice, one needs $B_P \gtrsim 0.3$ gauss for the largest expected stellar UV fluxes.

Finally, we can estimate κ in terms of the incident UV flux. Ignoring advection in equation (15) and neglecting collisional ionization (which is known to be sub-dominant – see Murray-Clay et al. 2009). Then equation (15) can simply be expressed by balancing the number of incoming photons with the number of recombinations such that:

$$\frac{F_{UV}}{h\nu_{13.6}} = \int_0^\infty n^2 \alpha_r d\ell \quad (47)$$

where ℓ is a ray extending from the star to the planet. If we consider the ray reaching the sub-stellar point of the planet, and drop the contribution from the Φ_c term, then equation (37) can be used to express the number density n in the form

$$n(\xi) = \left(\frac{P_0}{\mu_{\text{mmw}} a_s^2} \right) \exp \left[\Phi_g \left(\frac{1}{\xi} - 1 \right) \right], \quad (48)$$

where μ_{mmw} is the mean molecular weight ($\mu_{\text{mmw}} = 0.5 m_h$ for a gas consisting of pure ionized hydrogen gas). Thus, for the sub-stellar point, equation (48) may be written as

$$\frac{F_{UV}}{h\nu_{13.6}} = \alpha_r \left(\frac{P_0}{\mu_{\text{mmw}} a_s^2} \right)^2 R_P \int_1^\infty \exp \left[2\Phi_g \left(\frac{1}{\xi} - 1 \right) \right] d\xi. \quad (49)$$

The integral in equation (49) formally diverges due to the finite pressure at infinity, which arises because of the hydrostatic assumption. Such a finite pressure is not physical (e.g., Parker 1958) and the recombinations are expected to be dominant close to the planet in a realistic scenario. As a result, after truncating the integral after several scale heights, one finds that

$$\frac{F_{UV}}{h\nu_{13.6}} \approx \frac{\alpha_r}{2\Phi_g} \left(\frac{P_0}{\mu_{\text{mmw}} a_s^2} \right)^2 R_P, \quad (50)$$

where the result is independent of the truncation point. We can then cast κ in terms of the flux as

$$\begin{aligned} \kappa &\approx 50 \left(\frac{B_0}{1 \text{ gauss}} \right)^2 \left(\frac{F_{UV}}{10^4 \text{ erg s}^{-1}} \right)^{-1/2} \\ &\times \left(\frac{\Phi_g}{13} \right)^{-1/2} \left(\frac{R_P}{10^{10} \text{ cm}} \right)^{1/2}. \end{aligned} \quad (51)$$

Therefore, we expect $\kappa \gg 1$ for Hot Jupiters with moderate magnetic field strengths.

4.3 Volume of Loop Regions

The volume of the regions that support closed magnetic loops is another interesting quantity in this problem. For dipole field configurations, the volume of the loop region is given by an integral of the form

$$V = 4\pi \int_0^{\mu_m} d\mu \int_1^{\xi_x} \xi^2 d\xi, \quad (52)$$

where we have assumed azimuthal symmetry and $\mu = \cos \theta$. For the case of dipole fields, the loop reaches its point of maximum extent at the equator where $\theta = \pi/2$, and we have used the fact that the loops are symmetric with respect to the equatorial plane.

The largest magnetic loop that remains closed defines the outer boundary of the loop region. This loop intersects the planetary surface at $\xi = 1$ for polar angles given by μ_m , where $\mu_m = \cos \theta_m$, and reaches its point of maximum extent at dimensionless radius ξ_m . These defining quantities (μ_m , ξ_m) depend on the parameters of the problem as shown above. Note that the upper end ξ_x of the radial integration in equation (52) is given by the intersection of a ray (determined by the angular variable μ) with the outermost magnetic loop. Note that in general $\xi_m \neq \xi_x$.

The first integral can be immediately evaluated to obtain the form

$$V = \frac{4\pi}{3} \int_0^{\mu_m} d\mu (\xi_x^3 - 1). \quad (53)$$

The field line equation for dipole loops implies that the maximum extent of the loop is given by

$$\xi_m q = 1, \quad (54)$$

where $q = q_m$ is the coordinate that labels the largest magnetic loop (which defines the boundary of the loop region). We drop the subscript from here on to simplify the notation. With q specified, the critical values of the polar angle is determined by

$$q = 1 - \mu_m^2 \quad \text{or} \quad \mu_m^2 = 1 - q. \quad (55)$$

Next we note that the value of ξ_x is given by

$$\xi_x = (1 - \mu^2)/q. \quad (56)$$

Using these results, we can write the integral of equation (53) in the form

$$\begin{aligned} V &= \frac{4\pi}{3} q^{-3} \int_0^{\mu_m} d\mu \left[(1 - \mu^2)^3 - q^3 \right] \\ &= \frac{4\pi}{3} q^{-3} \left[(1 - q^3) \mu_m - \mu_m^3 + \frac{3}{5} \mu_m^5 - \frac{1}{7} \mu_m^7 \right]. \end{aligned} \quad (57)$$

We can use equation (55) to eliminate μ_m in favor of q , so that the expression becomes

$$\begin{aligned} V &= \frac{4\pi}{3} q^{-3} (1 - q)^{1/2} \\ &\times \left[(1 - q^3) - (1 - q) + \frac{3}{5} (1 - q)^2 - \frac{1}{7} (1 - q)^3 \right], \end{aligned} \quad (58)$$

which simplifies to the form

$$V = \frac{8\pi}{105} q^{-3} (1 - q)^{3/2} [8 + 12q + 15q^2], \quad (59)$$

Finally, we can write the volume in terms of the radial variable ξ_m to obtain

$$V = \frac{4\pi}{3} \xi_m^3 \cdot \frac{2}{35} (1 - \xi_m^{-1})^{3/2} [8 + 12\xi_m^{-1} + 15\xi_m^{-2}]. \quad (60)$$

Note that the first factor is the total spherical volume enclosed within the radius ξ_m , so that the second factor represents the fraction of this fiducial volume that is enclosed by the loop region.

5 NUMERICAL RESULTS

This section presents the results of our numerical simulations, which are divided into two classes. We first consider a set of simulations that allow for outflow over the entire planetary surface. More specifically, the goal of this initial set of models is to answer two questions: [1] To what extent does the flow wrap around the planet to the night side?, and [2] To what extent does the flow become sufficiently powerful to open up the dipole field of the planet? In order to isolate the effects of the magnetic field on the flow, these models do not include rotation or tidal fields (see Trammell et al. 2014 for the impact of these effects on the flow structure). As shown below in Section 5.1, however, flow from the surface is significantly suppressed from the night side of the planet because the magnetic fields inhibit zonal flows. As a result, we focus on the day side of the planet and present a survey of parameter space that considers only that hemisphere in Section 5.2.

5.1 Preliminary Full-Surface Simulations

This subsection presents results from a preliminary set of simulations that are designed to determine under what conditions the flow is able to wrap around the planet and/or disrupt the planetary dipole. Note that for this setup, with the planetary dipole pointing in the \hat{z} direction, and the star located along the positive x -axis, the problem is no longer axisymmetric. As a result, in order to simulate the flow with a 2D grid, we must make additional approximations. The flow is considered to be ‘pseudo-axisymmetric’, where each cell is *locally* forced to have flow properties such that $\partial_\phi = 0$ and there is no global requirement of axisymmetry, meaning we cannot include rotation (by performing a 2.5D simulation) which would introduce a non-physical shear along the poles. This obviously represents a restrictive situation and will only represent reality in the limit where the azimuthal flow is suppressed by the magnetic field (as is the case here). Of course, once the outflow from night-side of the planet is sufficiently small, the numerical treatment reduces to that of the simpler, day-side-only simulations. Thus, these simulations allow us to place constraints on what magnetic field strengths one must have before the flow can truly be well approximated an axisymmetric day-side only simulation, which we present in Section 5.2. Such a condition is implicitly assumed in previous studies (e.g. Adams 2011; Trammell et al. 2011, 2014) which we use these simulations to validate. We emphasise that in cases where there is a large scale azimuthal flow (situations where field lines could start on the day-side and end on the night-side, or vice-versa), then 2D simulations of this kind cannot be used and only full 3D simulations are appropriate.

These simulations use a Jupiter mass planet with radius $R_P = 10^{10}$ cm. The magnetic field strength on the planetary

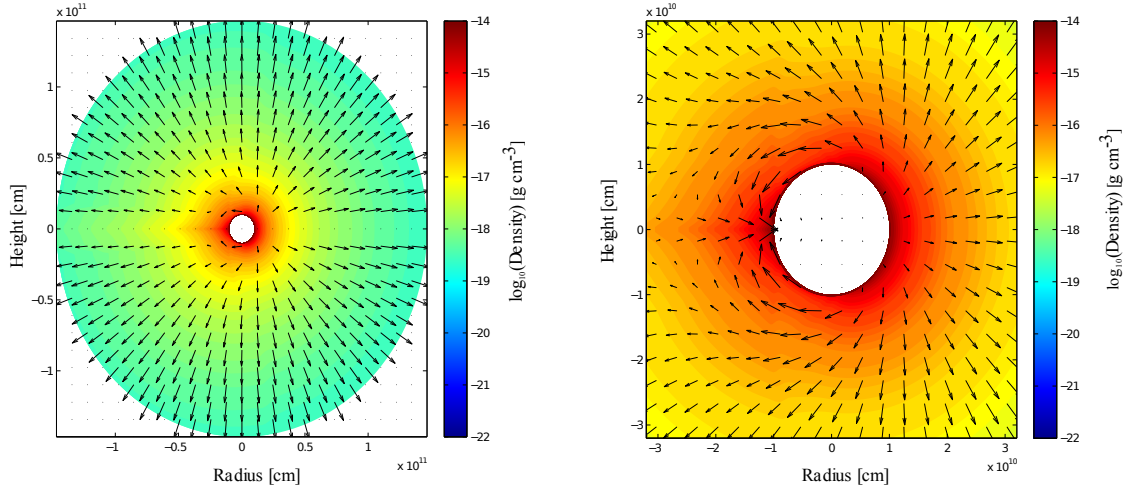


Figure 2. Outflow solutions including both the day and night sides of the planet with no magnetic field. The colour map shows the density and the vectors show the velocity field. The left-hand panel shows the full simulation domain and the right-hand panel shows a zoom-in on the planet. This model uses high levels of UV flux ($F_{UV} = 10^6 \text{ erg cm}^{-2} \text{ s}^{-1}$). The star is located along the positive x -axis. Note that the outflow can be launched from all longitudes of the planet, including the night side, in contrast to the case with a magnetic field (compare with Figure 3).

surface is taken to be $B_P = 0, 0.3$, and 3 gauss. The models are run with a background stellar magnetic field that is aligned with the pole of the planet and hence its dipole magnetic field. This configuration, which is consistent with the analytic study of Paper I, is specified by the parameter β_* , which is defined by equation (14). The value of β_* sets the ratio of the background field to that on the planetary surface. Here we take $\beta_* = 0, 0.003$, and 0.03 . The UV flux from the star is chosen to have values from the high end of the expected range, namely $F_{UV} = 10^5 - 10^6 \text{ erg cm}^{-2} \text{ s}^{-1}$, so that the flow becomes highly ionized and nearly isothermal with temperature $T = 10^4 \text{ K}$.

As shown in Figure 2, the flow wraps around the planet in the absence of a planetary field, i.e., the outflow can originate from essentially all longitudes. In addition, the outflow becomes nearly radial at the substellar point. In contrast, as shown in Figure 3, the presence of even a moderate magnetic field shuts down the outflow on the night side of the planet. The simulation illustrated by Figure 3 corresponds to a relatively weak planetary magnetic field ($B_P = 0.3$ gauss) and a large UV flux ($10^6 \text{ erg cm}^{-2} \text{ s}^{-1}$). Most of the expected regime of parameter space corresponds to stronger planetary fields and lower UV fluxes; we expect changes in both quantities to allow even less heat transport to the night side of the planet. As a result, for magnetically controlled flow, only the day side of the planet supports outflowing streamlines. This complication reduces the expected planetary mass outflow rates by a factor of ~ 2 . For the main survey of parameter space (see the following subsection), we thus confine the simulations to the day side of the planet.

The outflow can only take place along open magnetic field lines. As discussed in previous sections, field lines can be open for two reasons: [A] The pressure of the plasma at the planetary surface can open up field lines, and [B] The background field of the star can open up field lines (even in the absence of thermal pressure). In both cases, the

field lines are preferentially opened up along the poles. We want to understand the extent to which these two effects are operative.

5.2 Survey of Parameter Space

Given that the outflow is highly suppressed from the night side of the planet, we henceforth limit our simulations to the day side by performing axisymmetric simulations. This subsection presents results from a collection of simulations that surveys the relevant parameter space. Here we consider values of the field strength ratio $\beta_* = 0, 3 \times 10^{-4}, 1 \times 10^{-3}, 3 \times 10^{-3}, 1 \times 10^{-2}$ and 3×10^{-2} , with planetary surface magnetic field strengths of $B_P = 0.5, 1.0, 4.0$ and 10 gauss. The other important parameter is the UV flux, which is taken here to have large values of $F_{UV} = 10^5$ and $10^6 \text{ erg cm}^{-2} \text{ s}^{-1}$.

We demonstrate the effect of field opening from the pressure of the flow and the background vertical field in Figure 4, where we plot the flow topologies for simulations with a flux of $10^6 \text{ erg s}^{-1} \text{ cm}^{-2}$, our four magnetic field strengths ($0.5, 1, 4.0$ and 10 gauss from top to bottom) and β_* values of 0 and 3×10^{-3} (left to right). The first two columns show density and magnetic field topology while the second two columns show the plasma beta and velocity structure. Comparing models with different planetary field structures we see that at lower field strengths (and hence higher plasma betas) the evaporative flow is able to open out more and more closed field lines resulting in higher mass-loss rates. As one increases β_* a similar result is seen that the background field has opened out more field lines, resulting in mass-loss from an increased surface area of the planet's surface. We note for $B_P \lesssim 1$ gauss field opening due to the flow dominates over the background field, but for $B_P \gtrsim 1$ the number of opening field lines depends strongly on the strength (and also topology) of the background stellar field. The fraction

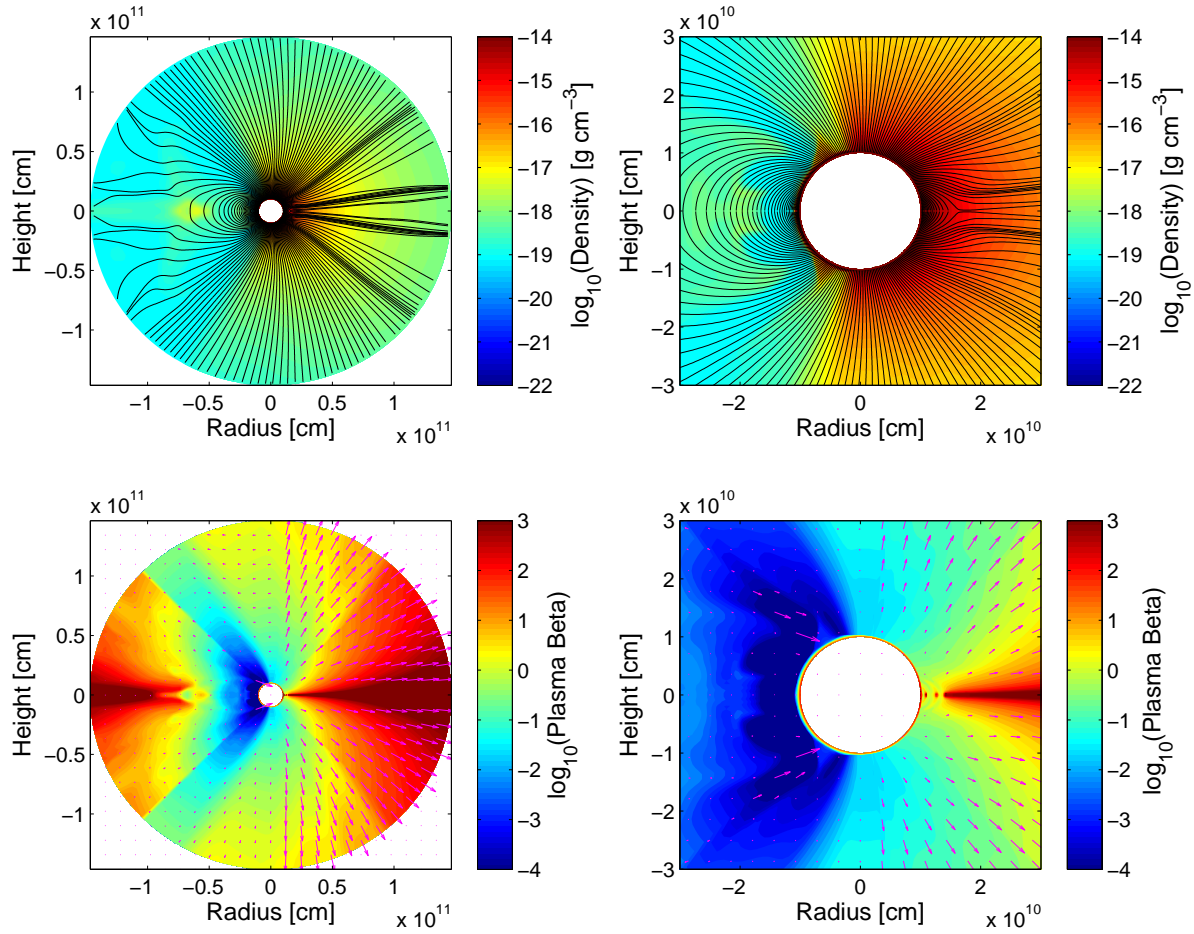


Figure 3. Outflow solutions including both the day and night sides of the planet with a moderate magnetic field strength on the surface ($B_P = 0.3$ gauss and $\beta_* = 0.0$) and UV flux of $F_{UV} = 10^6 \text{ erg s}^{-1} \text{ cm}^{-2}$. The top panels show the density and magnetic field structure; the bottom panels show the velocity structure and Plasma beta. The left-hand panels show the full simulation domain and the right-hand panels show a zoom-in on the planet. The star is located along the positive x -axis. Note that the outflow is primarily confined to the day side of the planet.

of the planetary surface that supports open field lines can be defined by $\sin^2 \theta_0$, where θ_0 is the polar angle of the last open field line (streamlines originating at smaller angles are closer to the pole and hence open).

Figure 5 shows the values of $\sin^2 \theta_m = q_m$ as a function of κ for the simulations. Since the numerical results for the pressure are not axisymmetric, and vary with latitude as well, the value of P_0 used to determine κ is taken to be the latitudinally averaged pressure at the ionization front (which is defined as the location where $X = 0.9$). The blue circles show the results for a purely dipole field (no background stellar field, or, equivalently, $\beta_* = 0$); the results closely follow the analytic predictions, as shown by the dashed curve in the figure (where the analytic result is shown for no rotation to be consistent with the simulations). The red squares show the results for $\beta_* = 0.003$ and the stars show results for larger $\beta_* = 0.03$. The fraction of the planetary surface that supports open field lines depends on both the pressure (defined via κ) and the background stellar field (defined via β_*). However, for $\beta_* = 0.01$, or larger, the background stellar

field provides the dominant contribution. Moreover, even for these high UV fluxes, all plausible magnetic field strengths will effectively control the structure of the planetary outflow.

Figure 6 shows the mass-loss rates from the simulations plotted as a function of the magnetic field strength on the planetary surface. Results are shown for a range of background stellar field strength and hence a range of $\beta_* = 0 - 0.03$, as well as the two values of UV fluxes. For one set of the simulations (with $\beta_* = 0.03$), the outflow does not reach a steady-state solution and we use a time-averaged mass-loss rate (see below for further discussion). For comparison, the mass-loss rates are shown for purely hydrodynamic flow (Murray-Clay et al. 2009; Owen & Jackson 2012)¹. The net result is simple: The inclusion of the magnetic field results in a clear suppression of the outflow rate, by approximately

¹ Since Murray-Clay et al. (2009) use a planet mass of $0.7 M_J$ and we use a planet mass of $1 M_J$, this comparison uses the results of Paper I to scale the results to our planet mass.

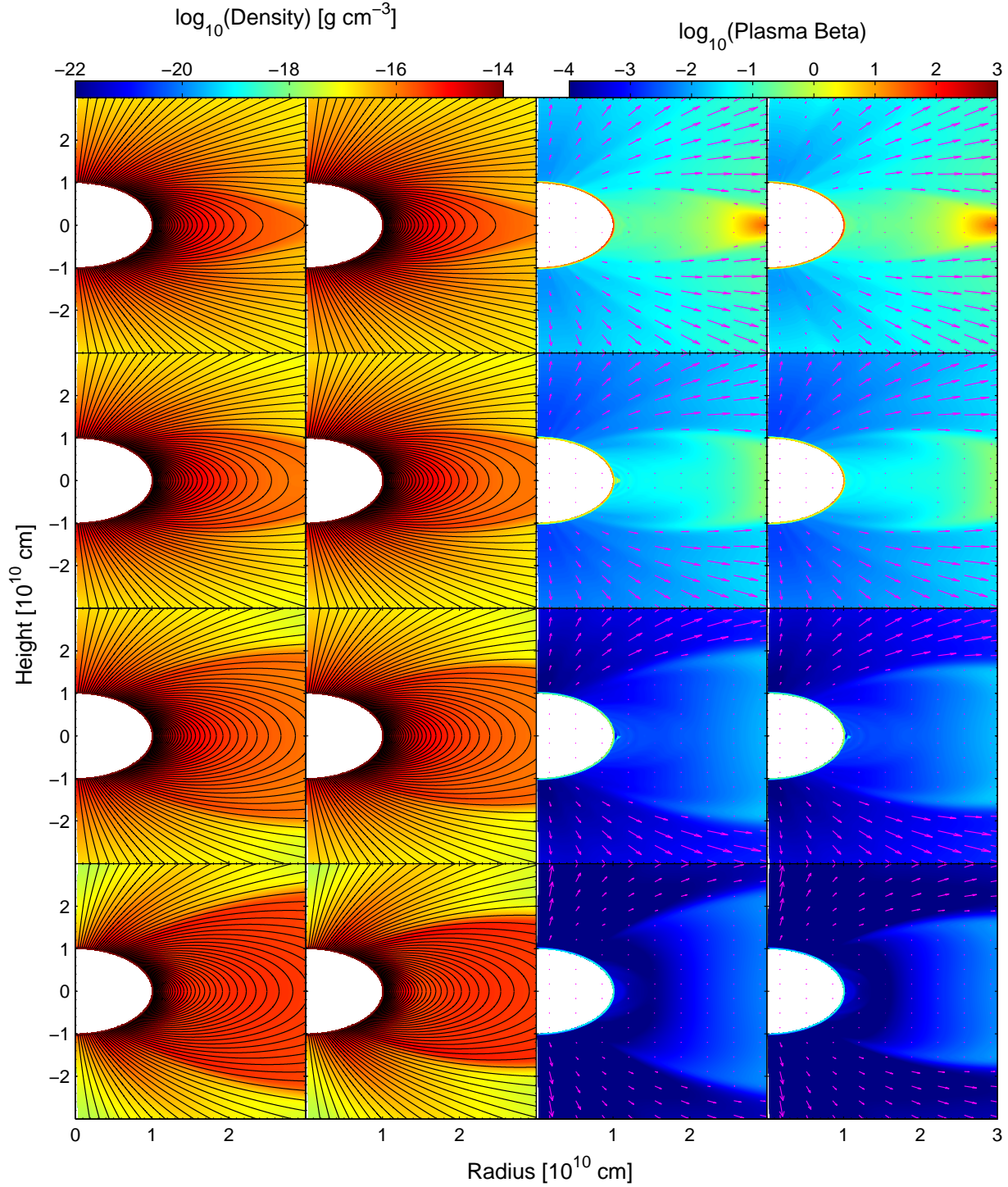


Figure 4. Flow structure and field topologies for a subset of our simulated parameter space. The rows represent planetary magnetic fields strengths of $B_P = 0.5, 1.0, 4.0$ & 10.0 from top to bottom. The first two columns show the density and magnetic field topology (first $\beta_* = 0$, second $\beta_* = 3 \times 10^{-3}$); the last two columns show the plasma beta and velocity structure (similarly: third $\beta_* = 0$, $\beta_* = 3 \times 10^{-3}$). Note that these panels show a zoom-in on the planet, whereas the full simulation domain extends out to $r = 1.5 \times 10^{11}$ cm (about 15 planetary radii). The star is located along the positive x-axis.

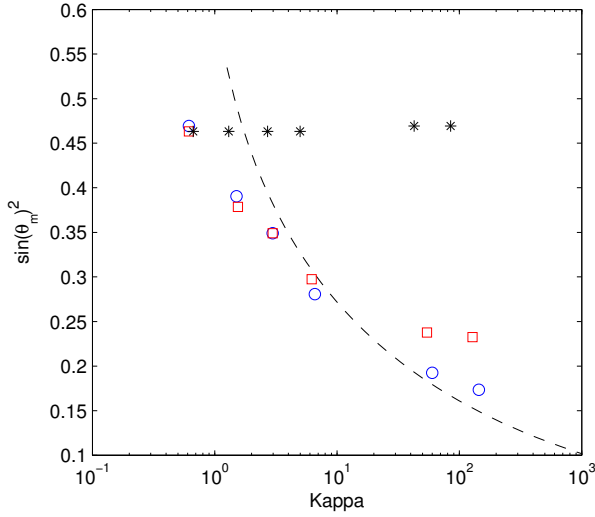


Figure 5. Latitude (θ_m) of the last open magnetic field line, and hence streamline, as a function of the parameter $\kappa = B_0^2/(8\pi P_0)$. The open circles show results for $\beta_* = 0$, the open squares for $\beta_* = 3 \times 10^{-3}$, and the stars are for $\beta_* = 3 \times 10^{-2}$. The dashed line shows the analytic result for $\beta_* = 0$ calculated in Section 4.1.

an order of magnitude. This suppression is not unexpected, as magnetic planets lose one factor of 2 because the night side flow is suppressed and another factor of $\sim 2-4$ because only a fraction of the field lines are open. In addition to the overall suppression, the outflow rate decreases with increasing magnetic field strength on the planetary surface. On the right hand side of Figure 6, the combination of the stellar and planetary magnetic fields control the geometry of the flow. On the left hand side of the figure, the fields are weak enough that some (additional) field lines are opened up by the plasma pressure, thereby increasing the outflow rate.

Figure 7 shows the mass-loss rates of the outflow as a function of planet mass. For this set of simulations, the planetary radius is held constant at $R_P = 10^{10}$ cm and the magnetic field strength is fixed at $B_P = 1$ gauss. The parameter β_* , which sets the strength of the background field due to the star, is also held constant at $\beta_* = 0.003$. Finally, the UV heating flux is fixed at a constant value of $F_{UV} = 10^6$ erg cm $^{-2}$ s $^{-1}$. These simulations show that the mass loss rate \dot{M} from the surface decreases with increasing planet mass in a nearly exponential manner. This general trend is consistent with the analytic prediction of Paper I (see their equation [65]). In this case, however, the UV fluxes are large, so that the low-mass planets have a larger fraction of their surface accessible to outflow. This trend is illustrated in Figure 8, which shows the quantity $\sin^2 \theta_m$, where θ_m is the polar angle of the last open field line (as discussed in section 4.2), as a function of planet mass. At the planetary mass increases, the outflow rate decreases, and fewer field lines remain open. Note that once the outflow rate falls to a sufficiently low value, the fraction of open field lines is determined primarily by the background field of the star (through the parameter β_* ; see equation [45]).

Another interesting trend found in the simulations is that for sufficiently large stellar contributions to the magnetic field (large values of β_*), the flow is suppressed further.

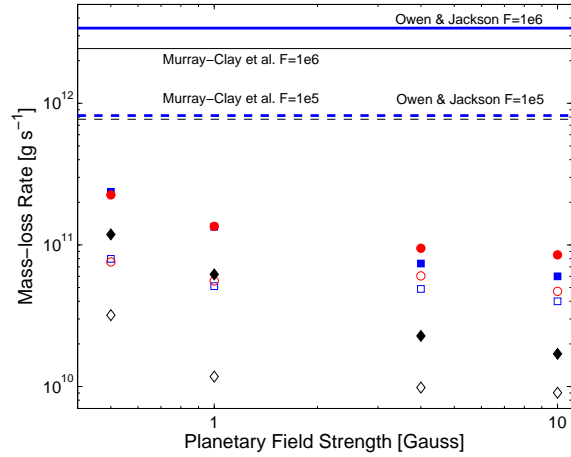


Figure 6. Mass outflow rates as a function of magnetic field strength on the planet. The open (filled) symbols correspond to the lower (higher) UV flux of $F_{UV} = 10^5$ (10^6) erg cm $^{-2}$ s $^{-1}$. The shapes of the symbols denote the value of the background stellar field, defined via $\beta_* = 0$ (squares), 0.003 (circles), and 0.03 (diamonds). The horizontal lines denote the mass outflow rates for planets with no magnetic fields (from: Murray-Clay et al. 2009-thin/black and Owen & Jackson 2012-thick/blue), where we have scaled these rates from $0.7 M_J$ in Murray-Clay et al. (2009) to $1 M_J$ using the scaling specified in Paper I. Note the Owen & Jackson (2012) rates also include a contribution from X-ray heating.

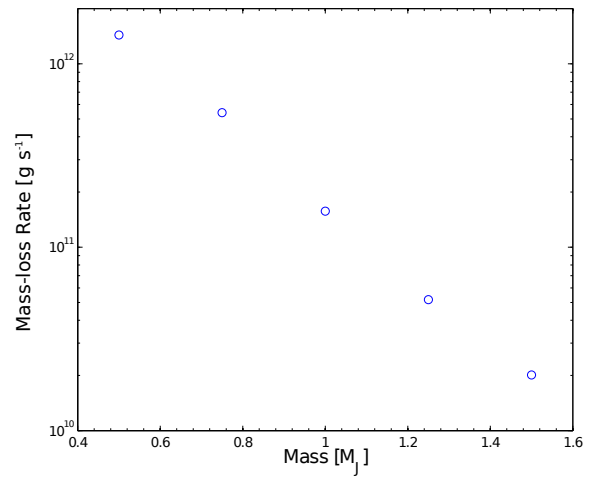


Figure 7. Mass outflow rates as a function of planet mass. Results are shown for $R_P = 10^{10}$ cm, $B_P = 1$ gauss, $\beta_* = 0.003$, and $F_{UV} = 10^6$ erg cm $^{-2}$ s $^{-1}$. The outflow rates show a nearly exponential decrease in \dot{M} with increasing mass, in keeping with analytic expectations.

This additional suppression occurs even though the fraction of the planetary surface that supports open field lines increases with β_* . This trend is shown in Figure 9, where we plot the mass-loss rate as a function of the parameter β_* for the set of simulations with $F_{UV} = 10^5$ erg s $^{-1}$ cm $^{-2}$, $B_P = 4$ gauss, and $M_P = 1 M_J$. Note that the mass loss rate rises slowly with increasing β_* , but then drops significantly for

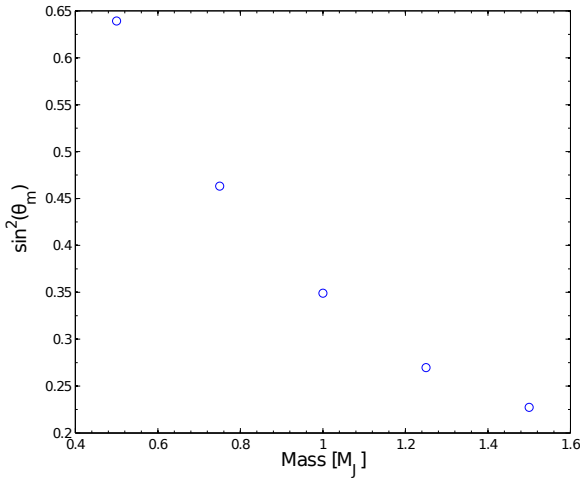


Figure 8. Opening angle for outflow models as a function of planet mass. Results are shown for $R_P = 10^{10}$ cm, $B_P = 1$ gauss, $\beta_* = 0.003$, and $F_{UV} = 10^6$ erg cm $^{-2}$ s $^{-1}$.

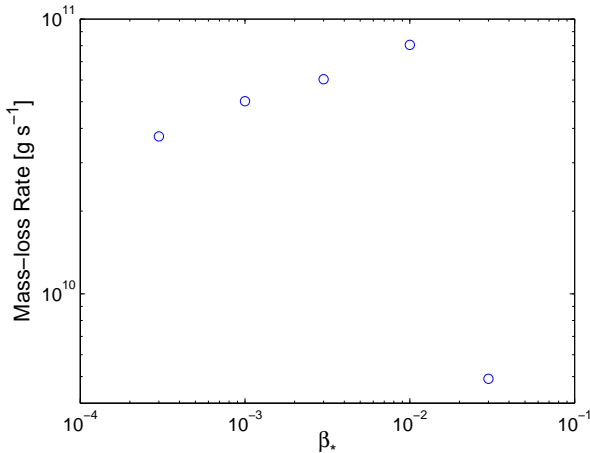


Figure 9. Mass-loss rate as a function of the background field strength (encapsulated by the parameter β_*). The set of simulations shown here uses $F_{UV} = 10^5$ erg s $^{-1}$ cm $^{-2}$, $B_P = 4$ gauss, and $M_P = 1$ M $_J$. The abrupt drop-off in the outflow rate occurs at large β_* because the flow cannot pass smoothly through the sonic point for all of the open field lines (see text).

$\beta_* > 10^{-2}$. Paper I predicts this type of behaviour: The initial rise occurs because larger values of β_* lead to more open field lines; the subsequent drop-off occurs because the flow cannot always pass smoothly through the sonic point along all of the open field lines. However, the suppression found here seems to be somewhat larger than that indicated by Paper I and warrants further study.

On a related note, for sufficiently large values of the parameter β_* (which sets the strength of the background stellar field), the simulations show that the flow does not always reach a steady state. Instead, the mass loss rate varies with time. Along some field lines, the flow is observed to alternate between the outward and inward directions, i.e., it displays an apparently oscillatory behaviour. This trend is

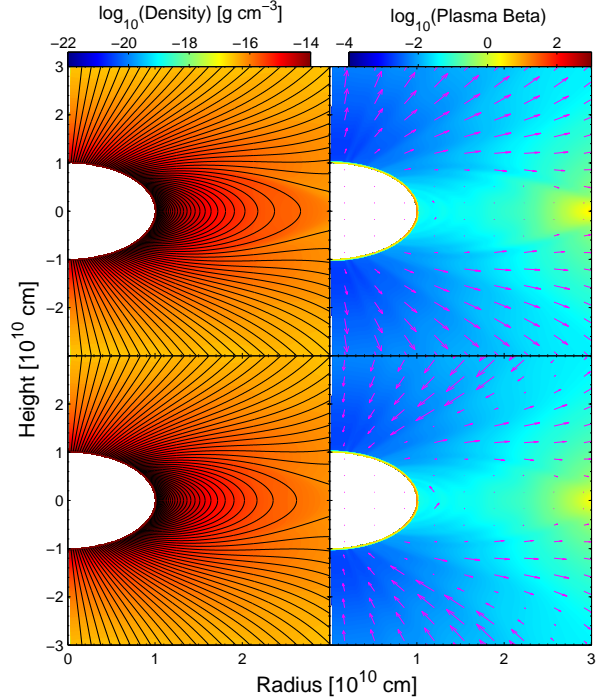


Figure 10. Flow topology for the simulation with $B_P = 1$ gauss, $\beta_* = 3 \times 10^{-2}$ and $F_{UV} = 10^6$ erg s $^{-1}$ cm $^{-2}$. The top panels show outflow along all open field lines, while the bottom panels show outflow along some open field lines and inflow along others; the time between the two snapshots is ~ 6 days. The left-hand column shows the density and magnetic field topology, whereas the right-hand column shows the plasma beta and velocity structure. The star is located along the positive x-axis.

demonstrated in Figure 10 for the simulation with $B_P = 1$ gauss, $\beta_* = 3 \times 10^{-2}$, and $F_{UV} = 10^6$ erg s $^{-1}$ cm $^{-2}$. For this case we find a variability time-scale of ~ 6 days, and the Figure shows two snapshots of the flow fields separated by 6 days. The magnetic field structure (depicted by the panels on the left side of the figure) does not change, consistent with magnetically controlled flow. On the other hand, flow along some field lines switches direction over the 6-day interval.

Further, the flow generally does not reach the sonic point, but instead remains subsonic. The flow in this regime is much more difficult to simulate than the case of steady, super-sonic winds. Because the flow is subsonic, and even travels inward along some streamlines (field lines) at some times, information can propagate from the outer boundary of the simulation volume into the flow region. Therefore, the results – in particular the variability time-scale – will be sensitive to the conditions at the outer boundary, where the outer boundary conditions used are only exact for super-sonic outflow (Stone & Norman 1992a).

6 CONCLUSION

This paper has considered mass loss from Hot Jupiters in the regime where the flow is magnetically controlled, including both numerical simulations and supporting analytic calculations. This section presents a summary of our results

(Section 6.1), a discussion of their implications, and some recommendations for future work (Section 6.2).

6.1 Summary of Results

This work shows that essentially all outflows from Hot Jupiters are expected to be magnetically controlled (provided that they support magnetic fields of moderate strength, $B_P \gtrsim 1$ gauss). This conclusion follows both from analytic considerations (see Section 2) and from detailed numerical simulations (see Section 5). Our simulations considered the most extreme cases, those with the largest expected stellar UV fluxes and moderate planetary fields strengths. Even in this regime, however, the magnetic field lines guide the flow and experience a negligible back reaction.

The inclusion of magnetic fields leads to suppression of the total mass outflow rate in three different ways. The first reduction arises because the field suppresses zonal winds on the planet, so that heat is not efficiently carried from the day side of the planet to the night side (compare Figures 2 and 3). The net effect is to essentially shut off the outflow from the night side of the planet and thereby reduce the total outflow rate by a factor of two.

The next type of suppression arises because not all magnetic field lines can be opened up, so that only a fraction of the planetary surface gives rise to outflow (see Figure 5). For the case of no background magnetic field from the star, the heated plasma must produce a greater pressure than the magnetic pressure and only the field lines close to the pole are open (see equation [44]). In the presence of a background stellar field, a larger fraction of the planetary surface supports outflow, but the active region is (again) confined to the poles (see Paper I and equation [45]). This effect reduces the overall outflow rate by another significant factor ($2 - 10$), which depends on the strength of the planetary field, the background stellar field, and the plasma pressure.

The third source of outflow suppression arises because not all open field lines allow the flow to make a smooth transition through the sonic point. The degree to which this effect reduces the outflow rates depends sensitively on the magnetic field geometry and other factors. This effect is most pronounced for strong background fields, which also act to open up more field lines (again see Paper I). As a result, stronger background fields lead to competing effects of more open field lines (implying more outflow) and difficulty in making the sonic transition (implying less outflow).

With the inclusion of the magnetic fields, the overall mass outflow rates are thus significantly smaller than indicated by previous work. Although the results depend on system parameters, over the regime considered here, outflow rates for planets with magnetic fields are about an order of magnitude smaller than those from planets with no magnetic fields (see Figure 6), and hence (about) an order of magnitude smaller than the simple estimates like that of equation (1).

The outflow rates decrease sharply with increasing planet mass, as expected. This trend is nearly exponential, as shown in Figure 7, and in agreement with analytic expectations (see equation [64] of Paper I).

Finally, our simulations show that the outflows have time dependent behavior in some portions of parameter space (Figure 10). Our working hypothesis is that the flow

cannot make a smooth transition through the sonic point in this regime, so that the flow solutions must vary with time (thereby resulting in non-steady flow). The general finding of non-steady flow under these conditions is consistent with the analysis of Paper I. Since the flow tends to be subsonic in this regime the outer boundary condition can influence the nature of the flow. This complication must be addressed in future work (see also the discussion below).

6.2 Discussion and Future Work

This work poses a number of interesting issues. First, we reiterate that planetary outflows are expected to be magnetically controlled, even for relatively weak fields ($B_P \sim 1$ gauss) and enormous UV fluxes from the star ($F_{UV} = 10^6$ erg cm⁻² s⁻¹). Moreover, the nature of the outflows (including mass loss rates and flow patterns) must ultimately depend on the geometry of the magnetic field, including the background contribution from the star. As a result, in order to understand planetary outflows, much more work must focus on the magnetic field configurations (see Section 2 for a discussion of the range of possible configurations).

On a related note, the problem of planetary outflows naturally divides into two regimes, the launch of the outflow and the subsequent propagation of the flow after it passes through the sonic point. Whereas this paper focuses on the launch of the outflow, the second part of the problem remains largely unexplored. After the outflow leaves the immediate vicinity of the planet, the flow structure depends on the details of the stellar wind, the stellar magnetic field, and the interactions of these fields with the planet (the dimensionless parameters that define the regimes of interest are outlined in Section 2). If the stellar magnetic fields are sufficiently strong near the planet, the planetary fields will connect up with the background stellar field, which will control the outflow away from the planet surface. On the other hand, if the stellar wind overwhelms the stellar magnetic field before reaching the planet, then a magnetospheric structure, similar to that seen for Earth and Jupiter in our Solar System, will develop. In either case, however, the characteristics of the stellar wind and/or stellar magnetic field will determine the eventual structure of the outflow.

To date, most of the work carried out on planetary outflows has focused on steady-state flow. Nonetheless, the results of our numerical simulations indicate that the flow can be time-dependent. The (relatively brief) discussion of this paper focuses on time-dependence that arises from the difficulty that the flow faces in passing smoothly through the sonic point (as anticipated in the analytic treatment of Paper I). However, a full treatment of this issue remains to be carried out, and the results must ultimately depend on the background stellar wind and stellar magnetic field configurations. Further, these time-dependent outflows can be subsonic, resulting in so-called breeze solutions. Unlike the case of transonic flows, where the launch of the outflow is largely decoupled from such outer properties, information can propagate inward through subsonic flows (toward the planetary surfaces) from large distances, so the background environment of the planet must play a role. In practice, this property implies that the outer boundary conditions can affect subsonic outflows originating from the planet surface.

In addition to the problem of passing through the sonic

point, time-dependent flow can arise from other sources. One interesting case is that of planets executing eccentric orbits, where the distance from the star varies appreciably over time. The UV heating rate will thus vary over the orbit and the strength of the outflow will depend on time. For this configuration, one can calculate the thermal time scale of the outflow, i.e., the time required for the UV heating flux to provide the thermal energy of the outflow within the sonic surface, which is comparable to the kinetic energy. To leading order this time scale can be written in the form

$$t_{\text{th}} = \frac{\int \rho v^2 dV}{\pi R_P^2 F_{\text{UV}}} \approx \frac{\dot{M} a_s}{\pi R_P F_{\text{UV}}} \approx 10^3 - 10^4 \text{ s}, \quad (61)$$

where we have used a moderate UV flux of $1000 \text{ erg cm}^{-2} \text{ s}^{-1}$ and we ignore factors of order unity. Although the time scale will vary substantially from system to system, typical values range from 20 minutes to a few hours. The time required for the outflow to change its properties can thus be much shorter than the orbital period, thereby allowing for the possibility of observing time-dependent outflows in eccentric systems. Note that the thermal time scale of equation (61) is roughly comparable to the sound-crossing time of the subsonic region $t_s = \text{few} \times R_P/a_s$. This convergence arises because the mechanical luminosity of the outflow is roughly the same as the rate of energy absorption from UV radiation. In practice, however, some losses occur and $t_s > t_{\text{th}}$.

Thus far, planetary outflows are only observed in two systems, although additional observations should be forthcoming. In addition to measuring the outflow rate, however, additional observational signatures must be developed. In order to solve for the flow properties, one must take into account the detailed heating and cooling mechanisms. This information, in turn, determines the possible emission lines produced in the outflow. If one solves for the chemistry of the outflow region, between the planetary surface and the surface where the flow becomes optically thin at UV wavelengths, then the absorption features can be determined. Finally, we (again) note that the magnetic field controls the flow over the entire region where the outflow can be observationally detected. As a result, the UV should display a polarization signal (although such measurements are difficult; see, e.g., Wiktorowicz 2009 for further discussion).

Mass loss from the planet can ultimately affect the spin rate of the planet (in the absence of other torques). Since the mass loss is asymmetric, taking place only on the day side of the planet, the flow itself can carry away angular momentum. In addition, however, magnetic torques associated with the magnetic stresses guiding the planetary outflow will play a role (Weber & Davis 1967). In this case, the magnetic torques will generally be dominant, by approximately the ratio of the magnetic pressure to the ram pressure of the outflow (see Section 2), i.e., by a large factor. Nonetheless, both types of torques should be studied in the future, as they can influence the planetary spin rate and perhaps even the orbital angular momentum.

Finally, we note that the present study has focused on planets with Jovian masses, where the escape speed from the surface is large enough so that the outflow rates are relatively small. To put this statement in context: Using the results shown in Figure 7, a $1.0 M_J$ planet has an outflow rate $\dot{M} \approx 10^{11} \text{ g/s}$, which turns out to be about $0.0016 M_J/\text{Gyr}$. With these low mass loss rates the planetary mass will

not change much over its lifetime. For planets with smaller masses, however, the outflow rates can be large enough to affect planetary masses. If we extrapolate the trend shown in Figure 7 down to the mass M_N of Neptune, the mass loss rate is about $3.15 M_N/\text{Gyr}$, large enough to make an enormous difference. As the planet mass decreases, the outflow rates increase and the amount of mass loss required to affect the planet decreases. As a result, we expect a type of cross-over mass such that larger planets are only moderately affected by mass-loss and smaller planets are efficiently evaporated down to their rocky cores or ocean surfaces (a similar threshold has been suggested by Owen & Wu 2013). This work indicates that the mass threshold will depend on the magnetic field structure of these intermediate-mass planets. A crucial question is thus whether or not close-in planets with mass comparable to Neptune will support moderately strong magnetic fields.

ACKNOWLEDGMENTS:

We are grateful to the referee for a constructive report that helped improve the manuscript. We would like to thank Marcelo Alvarez, Barbara Ercolano and Garrelt Mellema for helpful discussions. The numerical calculations were performed on the Sunnyvale cluster at CITA, which is funded by the Canada Foundation for Innovation. We are grateful for the hospitality of both CITA and the University of Michigan for visits that helped facilitate this collaboration.

APPENDIX A: RADIATIVE TRANSFER AND RAY TRACING

Our problem possess the two challenging aspects commonly encountered in radiation-hydrodynamics. Firstly, our ray-tracing scheme must be performed in a causal manner (Mellema et al. 2006 as the attenuation is strongly linked to the ionization structure, which in turn depends on the level of attenuation). Secondly the symmetry of the radiation field (plane-parallel) does not match the symmetry of the planet's atmosphere (\sim spherical). One could solve the second problem by performing the calculations on a Cartesian grid; however, setting up a spherical planetary atmosphere in Cartesian grid is problematic: it requires a large number of cells in the vicinity of the planet; ZEUS's directionally-split MHD algorithm may result in spurious numerical artefacts resulting from strong gradients inevitably mis-aligned with the grid, and finally it makes defining a boundary condition below the planet's atmosphere difficult.

Therefore, for maximum accuracy at minimal computational cost in the MHD scheme we choose to evolve our problem on a spherical grid and perform plane parallel ray-tracing through a spherical grid. Casting a single ray for every cell is prohibitively expensive so we develop a hybrid-characteristics scheme. Such a scheme (for the reverse problem of spherical ray-tracing on a Cartesian grid) has been shown to be accurate, efficient and parallelisable and scalable over MPI by Rijkhorst et al. (2006). The essence of the scheme is to decompose the grid into small 'blocks'. Within each of these blocks one performs a long characteristics ray-tracing calculation for every cell in the block. In between

the blocks the optical depths are interpolated onto the new rays using the method of short-characteristics; as such it is not as diffusive as a fully short-characteristics based scheme while still being computational feasible.

We follow Rijkhorst et al. (2006), such that within each block we perform a ray-tracing calculation for each cell and each cell corner on which short-characteristic interpolation takes place. The ray-structure is schematically shown in Figure A1. Thus, referring to the right-hand panel of Figure A1, the optical depth at the beginning of ray ‘A’ would be determined by bi-linear interpolation on the radial cell boundary using the optical-depths at the ends of rays ‘B’ and ‘C’; furthermore, the optical depth at the beginning of ray ‘D’ would be determined by bi-linear interpolation on the angular cell boundary using the optical depths at the end of rays ‘E’ and ‘B’. Such a scheme is particularly amenable to parallelisation in MHD codes that are already parallelised in a block-domain-decomposition manner (such as ZEUS). If the decomposed blocks for the ray-tracing scheme fit evenly within the blocks of the MHD scheme then non-local transfer of an information along an individual ray is not required between CPU’s. The ray-tracing is then performed in a casual manner where we step through the blocks (and cells within a block) such that the ionization structure of all previous cells any given ray intercepts is calculated before the ionization structure of any given cell is calculated (e.g. Mellema et al. 2006).

In all our calculations we decompose the 2D grid into ‘blocks’ of size 8×8 , which we find gives a good balance between accuracy and performance. It is unclear whether such a scheme is suitable for implementation in a 3D code, or whether a ray-splitting approach is more appropriate (e.g. Wise & Abel 2011) and will be investigated in future work.

APPENDIX B: NUMERICAL APPROACH

In order to study the evaporation of hot Jupiter atmospheres we have developed an ionization radiative transfer method for the well known ZEUS-MPV2 astrophysical MHD code (Stone & Norman 1992a,b; Hayes et al. 2006). The ZEUS code is a robust and well tested MHD code, where the magnetic field is evolved using ‘constrained transport’ (Evans & Hawley 1988) which preserves $\nabla \cdot \mathbf{B} = 0$ to machine precision provided the magnetic field is initialised with $\nabla \cdot \mathbf{B} = 0$. We choose to reconstruct fluxes at cell boundaries in a second order fashion using a Van-Leer limiter and the artificial viscosity is chosen such that discontinuities in the flow are smoothed over approximately two cells ($q = 2.0$). In several of the update sub-steps it was necessary to replace the finite-difference operators with appropriate finite-volume operators. In particular, this was necessary for the simulations with both the day and night-side (see Hayes et al. 2006, Appendix B2). In order to model the evaporation of hot Jupiters due to Ionizing EUV radiation we need to include a radiative transfer scheme that solves for the radiation field in a given cell, the ionization structure and gas temperature. Our scheme is separated in two main components: a scheme that solves for the ionization and thermal structure of a given cell and a ray-tracing scheme that captures the transport and attenuation of EUV photons (previously discussed in Appendix A).

The evolution of the ionization structure is governed by equation (15). We follow ZEUS’s natural structure and solve equation (15) using operator splitting, by splitting it into a ‘source’ step and a ‘transport’ step. In the source step we ignore the advection term and simply solve the equation

$$\frac{\partial X}{\partial t} = (1 - X)(\Gamma + n_e C) - X n_e \alpha_r. \quad (\text{B1})$$

In the transport step we account for the passive advection of electrons, ions and neutral species. ZEUS provides a built-in feature to perform this update and this is performed as (see Hayes et al. 2006, for details),

$$\frac{d}{dt} \int_V \rho_i dV = - \oint_{\partial V} \rho_i \mathbf{v} \cdot d\mathbf{S}, \quad (\text{B2})$$

where ρ_i is the mass density of the advected species, V is the cell volume, $d\mathbf{S}$ is the cell surface area element and \mathbf{v} is the gas velocity. Operationally, we update equation (B1) after the usual ZEUS body-force and artificial viscosity steps as well as updating the gas temperature and update equation (B2) after the ZEUS constrained transport and transport steps.

B1 Ionization and Thermal balance

We make the common On-The-Spot approximation, i.e., we assume that the recombinations to the ground state are locally reabsorbed (e.g., Spitzer 1978; Mellema et al. 2006; Gritschneder et al. 2009). As a result, for an ionizing flux entering a cell we can update the ionization/thermal structure of the cell, along with calculating the ionizing flux leaving the cell (required to give the ionizing flux entering the next cell). Our ionization scheme is based on the C2RAY/DORIC scheme (Mellema et al. 2006) and our thermal update is similar to that used in the IVINE code (Gritschneder et al. 2009). The C2RAY scheme solved many of the problems arising from ionization radiative transfer in hydrodynamic simulations (Mellema et al. 2006), particularly problems associated with photon conservation, sharp ionization fronts, and the propagation of rapidly moving R-type fronts (not an issue for our problem). Because the C2RAY scheme is described in detail in Mellema et al. (2006), only the basics are presented here. For simplicity, we only consider hydrogen so that the evolution of the ionized fraction (X) is given by

$$\frac{\partial X}{\partial t} = (1 - X)(\Gamma + nXC) - nX^2\alpha_r. \quad (\text{B3})$$

In the On-The-Spot approximation the recombination rate is simply the Case B recombination coefficient (α_b) given by (e.g. Mellema et al. 2006)

$$\alpha_b = 2.59 \times 10^{-13} \text{ cm}^3 \text{ s}^{-1} \left(\frac{T}{10^4 \text{ K}} \right)^{-0.7}. \quad (\text{B4})$$

Equation (B3) can be solved iteratively using the method suggested by Schmidt-Voigt & Koeppen (1987), where one takes Γ , $n_e = Xn$, C , and α_b to be constant over a time step such that equation (B3) has the solution

$$X(t + \Delta t) = X_{\text{eq}} + [X(t) - X_{\text{eq}}] \exp\left(-\frac{\Delta t}{t_{\text{ion}}}\right), \quad (\text{B5})$$

where we have defined

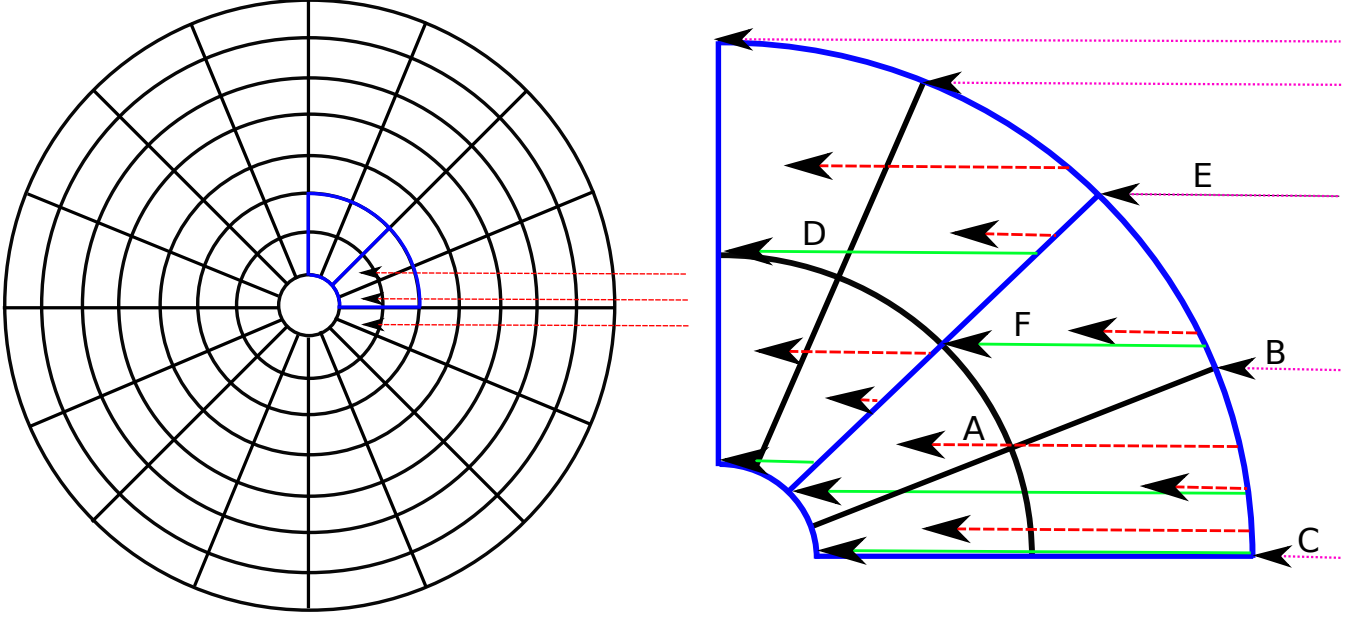


Figure A1. Schematic diagram showing how the hybrid-ray tracing scheme works in practice for plane-parallel radiative transfer on a spherical grid. The left hand panel shows how we decompose the grid into smaller ‘blocks’, indicated by the blue highlighted grid structure. The right-hand panel shows a zoom-in of an individual block and shows all of the associated rays present in the calculation. The dotted rays are those originating in previous blocks, which are required for the interpolation scheme used to calculate the starting optical depths for the rays in this block. The dashed rays show the rays calculated for every cell in this block. The solid rays indicate all of the extra rays needed for the interpolation in the next block to calculate the starting optical depths. The letter labels are used in the text to describe the interpolation scheme.

$$t_{\text{ion}} = \frac{1}{\Gamma + n_e C + n_e \alpha_b} \quad (\text{B6})$$

and

$$X_{\text{eq}} = \frac{\Gamma + n_e C}{\Gamma + n_e C + n_e \alpha_b}. \quad (\text{B7})$$

The values of Γ , $n_e n$, C , and α_b can then be recalculated using the new ionization state and equation (B5) can be evaluated again and so-forth. The essence of the iteration scheme is to repeatedly solve equation (B5) where t_{ion} and X_{eq} are replaced with *time-averaged* quantities, which are updated using the previous ionization structure of the cell and the value at the current iteration, until convergence is achieved and t_{ion} and X_{eq} represent the correct time-averaged quantities. The advantage of such an iteration procedure is it readily provides an analytic formula for the time-average ionization fraction by time-averaging equation (B5).

During each iteration of equation (B5), we need to know the gas temperature. In reality this would require solving the thermal balance equations iteratively as well. However, since in this study we are restricting ourselves to the highest UV fluxes where the flow is close to recombination equilibrium (Murray-Clay et al. 2009), we can dramatically simplify the thermal balance problem. Since fully ionized gas has a temperature ($\sim 10^4$ K) we follow the method of Gritschneder et al. (2009) and adopt a gas temperature profile of

$$T = X T_{\text{hot}} + (1 - X) T_{\text{cold}}, \quad (\text{B8})$$

where we set $T_{\text{hot}} = 10^4$ K and $T_{\text{cold}} = 10^3$ K, where our choice of T_{cold} is approximately the temperature of the underlying bolometrically heated atmosphere (we note that this choice makes little difference to our results provided

that the scale height of the underlying atmosphere is much smaller than the planetary radius Murray-Clay et al. 2009; Owen & Jackson 2012). The internal energy of the gas is then found via an ideal equation of state, such that

$$u = \frac{1}{\gamma - 1} \frac{k_b (1 + X)}{m_h} \rho T, \quad (\text{B9})$$

where we choose $\gamma = 5/3$. This parametrization is valid only if the ionization front is small compared to the flow-scale; this constraint restricts our investigation to the highest UV fluxes experienced by hot Jupiters.

B2 Numerical Tests

Since we have not developed a new scheme from scratch, we restrict this discussion to a small number of test problems aimed specifically at our problem in hand. Thus, we perform 1D spherically symmetric flow calculations without magnetic fields. In this case the problem can be well approximated by the isothermal ‘Parker-wind’ problem which possesses an analytic solution for the velocity structure of the flow (Parker 1958). In Figure B1 we show the velocity structure resulting from our code compared to the ‘Parker-wind’ solution for a $1 M_J$ planet with a radius of $r_p = 10^{10}$ cm and UV flux of $10^5 \text{ erg s}^{-1} \text{ cm}^{-2}$. We note that the flow on the upstream side of the ionization front should match onto the Parker wind solution.

Secondly, in the recombination limit it is well known the density at the base of the ionization front should scale with the incoming flux as $n \propto F_{\text{UV}}^{1/2}$ (e.g. Spitzer 1978). Furthermore, assuming the structure to be hydrostatic (true for flows that are highly sub-sonic near the ionization front),

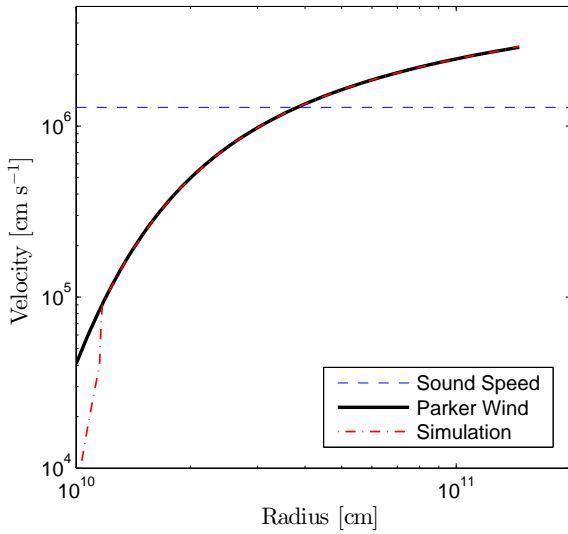


Figure B1. Figure showing the results of the Parker wind test, i.e., the flow speed as a function of radius for both the numerical and analytic solutions. After the flow passes through the ionization front, the velocity closely follows the analytic Parker wind solution (as expected).

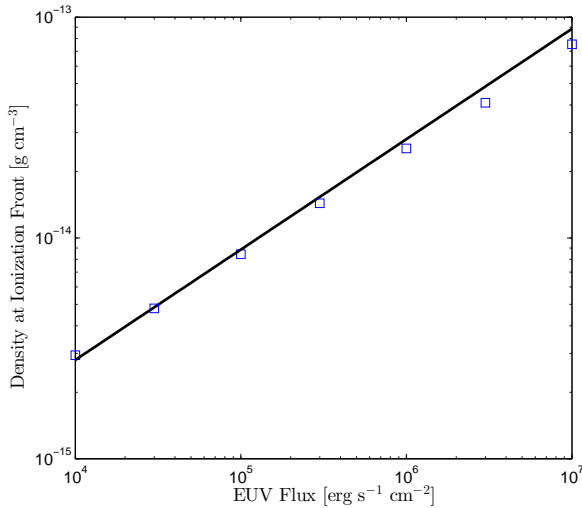


Figure B2. Figure showing the results of the ionization front test. The points show the simulated values (defined as the density at the location where the ionization fraction $X = 0.9$) and the solid line shows the analytic expectation given by equation (50).

one can calculate the density at the ionization front by assuming steady state in equation (B3). This is the expression evaluated in Section 4.2 and presented in equation (50). In Figure B2 we show the density at the ionization front (defined as $X = 0.9$) determined by the code compared to the analytical expectation.

We find that our radiative-transfer and ionization balance algorithm to be in-agreement with analytic expectations giving us confidence it is suitable for our evaporation

study presented. Finally, we perform several convergence tests: 1) we double the spatial resolution, 2) we double the size of our ‘blocks’ in the hybrid characteristics ray-tracing method detailed in Appendix A, 3) with half the size of our ray-tracing blocks. All these tests were performed on our $B_P = 1$ gauss, $\beta_* = 0$ and $F_{UV} = 10^6$ erg s $^{-1}$ cm $^{-2}$ calculation and show agreement to $\lesssim 5\%$, indicating our chosen resolution and ‘block’ size is appropriate for our calculations.

REFERENCES

- Adams, F. C. 2011, ApJ, 730, 27 (Paper I)
- Adams, F. C., & Gregory, S. G. 2012, ApJ, 744, 55
- Adams, F. C., Hollenbach, D., Laughlin, G., & Gorti, U. 2004, ApJ, 611, 360
- Baliunas, S., Sokoloff, D., & Soon, W. 1996, ApJ, 457, L99
- Banaszkiewicz, M., Axford, W. I., & McKenzie, J. F. 1998, A&A, 337, 940
- Baraffe, I., Alibert, Y., Chabrier, G., & Benz, W. 2006, A&A, 450, 1221
- Baraffe, I., Selsis, F., Chabrier, G., Barman, T. S., Allard, F., Hauschildt, P. H., & Lammer, H. 2004, A&A, 419, L13
- Black, J. H. 1981, MNRAS, 197, 553
- Blandford, R. D., & Payne, D. G. 1982, MNRAS, 199, 883
- Bodenheimer, P., Laughlin, G., & Lin, D.N.C. 2003, ApJ, 592, 555
- Boué, G., Figueira, P., Correia, A.C.M., & Santos, N. C. 2012, A&A, 537, L3
- Cohen, O., Drake, J. J., Kashyap, V. L., Saar, S. H., Sokolov, I. V., Manchester, W. B., Hansen, K. C., & Gombosi, T. I. 2009, ApJ, 704, 85
- Cuntz, M., Saar, S. H., & Musielak, Z. E. 2000, ApJ, 533, 151
- Donati, J.-F., Semel, M., Carter, B. D., Rees, D. E., & Collier Cameron, A. 1997, MNRAS, 291, 658
- Erkaev, N. V., Kulikov, Y. N., Lammer, H., et al. 2007, A&A, 472, 329
- Evans, C. R., & Hawley, J. F. 1988, ApJ, 332, 659
- García Muñoz, A. 2007, Planet. Space Sci., 55, 1426
- Ghosh, P., & Lamb, F. K. 1978, ApJ, 223, L83
- Ghosh, P., & Lamb, F. K. 1979, ApJ, 232, 259
- Gregory, S. G., Jardine, M., Simpson, I., & Donati, J.-F. 2006, MNRAS, 371, 999
- Gregory, S. G., Matt, S. P., Donati, J.-F., & Jardine, M. 2008, MNRAS, 389, 1839
- Gregory, S. G., Jardine, M., Gray, C. G., & Donati, J.-F. 2010, Reports on Progress in Physics, 73, 126901
- Gregory, S. G. 2011, Am. J. Phys., 79, 461
- Griesmeier, J.-M., Stadelmann, A., Penz, T., Lammer, H., Selsis, F., Ribas, I., Guinan, E. F., Mutschmann, U., Bierntat, H. K.m & Weiss, W. W. 2004, A&A, 425, 753
- Gritschneider, M., Naab, T., Burkert, A., et al. 2009, MNRAS, 393, 21
- Guenther, E. W., & Emerson, J. P. 1997, A&A, 321, 803
- Hartigan, P., Edwards, S., & Ghandour, L. 1995, ApJ, 452, 736
- Hayes, J. C., Norman, M. L., Fiedler, R. A., et al. 2006, ApJS, 165, 188
- Ip, W.-H., Kopp, A., & Hu, J.-H. 2004, ApJ, 602, L53
- Johns-Krull, C. M. 2009, IAU Symposium, 259, 345

- Khodachenko, M. L., Alexeev, I., Belenkaya, E., Lammer, H., Griemeier, J.-M., Leitzinger, M., Odert, P., Zaqarashvili, T., Rucker, H. O. 2012, *ApJ*, 744, 70
- Königl, A. 1991, *ApJ*, 370, L39
- Koskinen, T. T., Aylward, A. D., & Miller, S. 2007, *Nature*, 450, 845
- Koskinen, T. T., Cho, J. Y.-K., Achilleos, N., & Aylward, A. D. 2010, *ApJ*, 722, 178
- Koskinen, T. T., Harris, M. J., Yelle, R. V., & Lavvas, P. 2013, *Icarus*, 226, 1678
- Laine, R. O., Lin, D.N.C., & Dong, S. 2008, *ApJ*, 685, 521
- Lammer, H., Selsis, F., Ribas, I., Guinan, E. F., Bauer, S. J., & Weiss, W. W. 2003, *ApJ*, 598, 121
- Lanza, A. F. 2008, *A&A*, 487, 1163
- Lanza, A. F. 2009, *A&A*, 505, 339
- Lanza, A. F. 2012, *A&A*, 544, 23
- Laughlin, G., Crismani, M., & Adams, F. C. 2011, *ApJ*, 729, 7L
- Lecavelier des Etangs, A., Ehrenreich, D., Vidal-Madjar, A., Ballester, G. E., Désert, J.-M., Ferlet, R., Hébrard, G., Sing, D. K., Tchakoumegni, K.-O., & Udry, S. 2010, *A&A*, 514, 72
- Linsky, J. L., Yang, H., France, K., Froning, C. S., Green, J. C., Stocke, J. T., & Osterman, S. N. 2010, *ApJ*, 717, 1291
- Mellema, G., Iliev, I. T., Alvarez, M. A., & Shapiro, P. R. 2006, *New Astronomy*, 11, 374
- Murray-Clay, R. A., Chiang, E. I., & Murray, N. 2009, *ApJ*, 693, 23
- Osterbrock, D. E. 1989, Research supported by the University of California, John Simon Guggenheim Memorial Foundation, University of Minnesota, et al. Mill Valley, CA, University Science Books, 1989, 422 p.,
- Owen, J. E., Ercolano, B., Clarke, C. J., & Alexander, R. D. 2010, *MNRAS*, 401, 1415
- Owen, J. E., Clarke, C. J., & Ercolano, B. 2012, *MNRAS*, 422, 1880
- Owen, J. E., & Jackson, A. P. 2012, *MNRAS*, 425, 2931
- Owen, J. E., & Wu, Y. 2013, *ApJ*, 775, 105
- Parker, E. N. 1958, *ApJ*, 128, 664
- Parker, E. N. 1965, *Space Science Reviews*, 4, 666
- Preusse, S., Kopp, A., Büchner, J., & Motschmann, U. 2004, *A&A*, 434, 1191
- Radoski, H. R. 1967, *JGR*, 72, 418
- Rijkhorst, E.-J., Plewa, T., Dubey, A., & Mellema, G. 2006, *A&Ap*, 452, 907
- Romanova, M. M., Ustyugova, G. V., Koldoba, A. V., & Lovelace, R.V.E. 2002, *ApJ*, 578, 420
- Romanova, M. M., Ustyugova, G. V., Koldoba, A. V., Wick, J. V., & Lovelace, R.V.E. 2003, *ApJ*, 595, 1009
- Salat, A., & Tataronis, J. A. 2000, *J. Geophys. Res.*, 105, 13055
- Schmidt-Voigt, M., & Koeppen, J. 1987, *A&Ap*, 174, 211
- Shkolnik, E., Walker, G.A.H., Bohlender, D. A., Gu, P.-G., & Kürster, M. 2005, *ApJ*, 622, 1075
- Shkolnik, E., Bohlender, D. A., Walker, G.A.H., Collier Cameron, A. 2008, *ApJ*, 676, 628
- Shu, F. H. 1992, *Gas Dynamics* (Mill Valley: Univ. Science Books)
- Skumanich, A. P. 1972, *ApJ*, 171, 565
- Spitzer, L. 1978, *Physics Processes in the Interstellar Medium* (New York: Wiley)
- Stone, J. M., & Norman, M. L. 1992, *ApJS*, 80, 753
- Stone, J. M., & Norman, M. L. 1992, *ApJS*, 80, 791
- Stone, J. M., & Proga, D. 2009, *ApJ*, 694, 205
- Trammell, G. B., Arras, P., & Li, Z.-Y. 2011, *ApJ*, 728, 152
- Trammell, G. B., Arras, P., & Li, Z.-Y. 2014, *ApJ*, in press
- Vidal-Madjar, A., Lecavelier des Etangs, A., Désert, J.-M., Ballester, G. E., Ferlet, R., Hébrard, G., & Mayor, M. 2003, *Nature*, 422, 143
- Watson, A., Donahue, T., & Walker, J. 1981, *Icarus*, 48, 150
- Weber, E. J., & Davis, L. 1967, *ApJ*, 148, 217
- Weinreich, G. 1998, *Geometrical Vectors* (Chicago: Univ. Chicago Press)
- Wiktorowicz, S. J. 2009, *ApJ*, 696, 1116
- Wise, J. H., & Abel, T. 2011, *MNRAS*, 414, 3458
- Wood, B., Müller, H.-R., Zank, G., & Linsky, J., 2002, *ApJ*, 574, 412
- Woods, T. N., Rottman, G. J., Bailey, S. M., Solomon, S. C., & Worden, J. R. 1998, *Sol. Phys.*, 177, 133
- Wright, E. M. 1959, *Bull. Amer. Math. Soc.* 65, 89
- Yelle, R. V. 2004, *Icarus*, 170, 167